GEOPHYSICS, VOL. 80, NO. 4 (JULY-AUGUST 2015); P. KS51–KS68, 11 FIGS.
10.1190/GEO2014-0455.1

Noise-based monitoring and imaging of aseismic transient deformation induced by the 2006 Basel reservoir stimulation

Gregor Hillers[1], Stephan Husen[2], Anne Obermann[3], Thomas Planès[4], Eric Larose[1], and Michel Campillo[1]

ABSTRACT

We have analyzed the time-dependent properties of the ambient seismic wavefield between 0.1 and 8 Hz to detect, resolve, monitor, and image the deformation induced by the water injection associated with the stimulation of the 2006 Deep Heat Mining Project in the city of Basel, Switzerland. The application of passive methods allowed the detection of an aseismic transient of approximately 35 days' duration that began with the onset of the reservoir stimulation. Peak deformation was reached some 15 days after the bleed-off and after the induced seismicity ceased. We resolved a significant increase in seismic velocities and a simultaneous decorrelation of the noise correlation coda waveforms. The wavefield properties implied that the material response was monitored mainly in the sedimentary layer (<2.5 km) above the stimulated volume that was approximately 4.5 km deep. We inverted the velocity-change and decorrelation data to estimate the spatial distribution of the medium changes. The resulting images showed that the strong velocity variations and medium perturbations were generally colocated with the lateral distribution of the induced seismicity. Positive velocity changes and damage around the injection site indicated subsidence, settling, and compaction of the material overlying the stimulated volume. Our results demonstrate that noise-based analysis tools can provide important observables that are complementary to results obtained with standard microseismicity tools. Passive monitoring and imaging have the potential to mature into routinely applied observation techniques that support reservoir management in a variety of geotechnical contexts, such as for mining, fluid injection, hydraulic fracturing, nuclear waste management, and CO_2 storage.

INTRODUCTION

The physical and mechanical properties of a stimulated rock mass change in response to the engineering and geotechnical activities associated with mining, hydrocarbon production, hydraulic fracturing, waste storage, CO_2 capture and storage, and heat and water extraction or water injection. Fluid injections can result in changes in the local stress field that can trigger instabilities that lead to increased seismic risk in areas characterized by little or no natural seismicity (Giardini, 2009; Ellsworth, 2013). Geothermal applications and CO_2 sequestration efforts are likely to increase over the next few decades in response to the anticipated decline in conventional hydrocarbon availability and climate issues. Geophysical techniques that can be used to define a geothermal site include 3D seismic imaging, thermal gradient surveys, and well logging, as well as gravimetric, magnetic, and electric methods. In contrast, monitoring methods applied in reservoir management are mainly based on microseismicity (Shapiro, 2008). The properties of induced seismicity can provide estimates of hydraulic rock properties and local and regional stress fields and real-time assessments of seismic hazard (Shapiro et al., 2007, 2011; Bachmann et al., 2011). However, once a reservoir has matured and percolation networks are established, the induced seismicity greatly decreases, or it ceases altogether, and seismologists can no longer study the reservoir response (Schoenball et al., 2014). This includes aseismic deformation that can indicate potentially unwanted leakage and the

Manuscript received by the Editor 1 October 2014; revised manuscript received 27 February 2015; published online 25 June 2015.
[1]Université Joseph Fourier, Institut des Sciences de la Terre, CNRS, Grenoble, France. E-mail: gregor.hillers@ujf-grenoble.fr; eric.larose@ujf-grenoble.fr; michel.campillo@ujf-grenoble.fr.
[2]Kantonales Laboratorium, Kontrollstelle für Chemie und Biosicherheit, Basel, Switzerland. E-mail: stephan.husen@bs.ch.
[3]Swiss Seismological Service, ETH, Zurich, Switzerland. E-mail: anne.obermann@sed.ethz.ch.
[4]Colorado School of Mines, Department of Civil and Environmental Engineering, Golden, Colorado, USA. E-mail: tplanes@mines.edu.

corresponding contamination of aquifers (Rutqvist, 2012). For a constant assessment of reservoir properties, it is therefore important to develop and apply tools that perform independently of the spatiotemporally variable seismicity (Julian and Foulger, 2010).

Passive, or noise-based, methods based on the analysis of the ambient wavefield or seismic noise can potentially provide key complementary observables related to reservoir dynamics. These methods are based on the proportionality between the Green's function and the crosscorrelation function that can be constructed from diffuse seismic wavefields (Lobkis and Weaver, 2001; Wapenaar, 2004; Roux et al., 2005; Sánchez-Sesma and Campillo, 2006; Snieder, 2007). This principle has led to passive seismological imaging and monitoring applications (e.g., Campillo et al., 2011; Snieder and Larose, 2013), in which the resolution is governed by the properties of the coherent parts of the noise wavefield. Classic imaging techniques process timing and amplitude information associated with the direct (ballistic) arrival in crosscorrelation functions. Here, we focus on monitoring methods to track systematic changes in the crosscorrelation coda wavefield that are governed by variations in the elastic or scattering properties of the heterogeneous medium. In seismological contexts, these principles have been applied to resolve relative velocity changes between $O(0.01\%)$ and $O(1\%)$ associated with volcanic activity (Brenguier et al., 2008b; Obermann et al., 2013a), rapid (Wegler and Sens-Schönfelder, 2007; Brenguier et al., 2008a; Wegler et al., 2009; Hobiger et al., 2012; Froment et al., 2013) and slow (Rivet et al., 2011) slip on earthquake faults, water content in the shallow crust (Sens-Schönfelder and Wegler, 2006a; Meier et al., 2010; Froment et al., 2013; Hillers et al., 2014), thermal processes (Sens-Schönfelder and Larose, 2008; Richter et al., 2014; Hillers et al., 2015a), and tidal-induced deformation (Hillers et al., 2015b). Scattered wavefield sensitivity

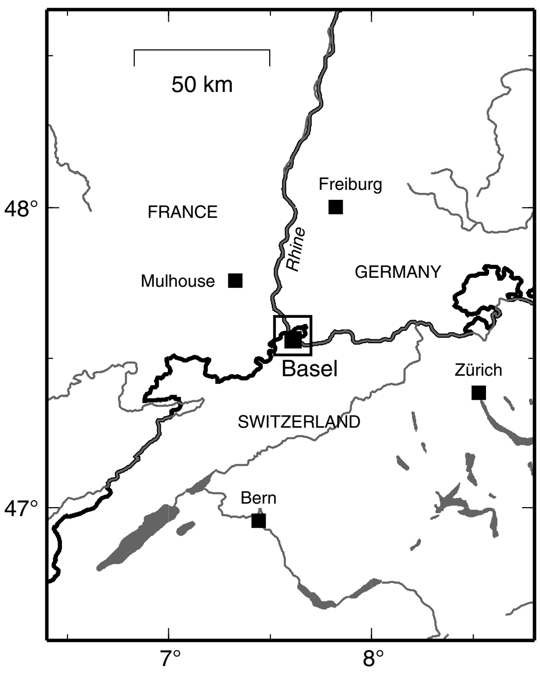

Figure 1. Location of the study area, as indicated by the black rectangle. Black and gray lines represent borders and major rivers, respectively. Throughout this study, the country and river names are given in English, and the city names are given in the language of the respective country.

allows imaging of static and transient variations in the properties of structural and mechanical media (Larose et al., 2010; Rossetto et al., 2011; Obermann et al., 2013a, 2014; Planès et al., 2015). This high sensitivity to medium changes warrants trial applications in geothermal and other geotechnical stimulation contexts (Obermann et al., 2015), thereby extending the applicability of passive surface-wave tomography of reservoir structures (e.g., Mordret et al., 2013).

Here, we investigate the use of passive methods to detect, resolve, monitor, and image deformation patterns associated with the 2006 Deep Heat Mining Project in Basel, Switzerland. This project constituted an effort to develop an enhanced geothermal system. The site within the city limits of Basel, located in the tri-border region of France, Germany, and Switzerland, is situated at the southern edge of the lower Rhine-Graben structure (Figure 1). A high heat-flow gradient associated with rifting facilitates the production of geothermal energy for domestic heating and hot water supplies. However, the temperature gradient still required a production depth of 4–5 km, where limited fluid percolation properties in the crystalline basement required the system to be enhanced. The reservoir was thus stimulated with a massive injection of approximately $12,000\ m^3$ of water beginning on 2 December 2006, at a depth of approximately 5 km, to open fractures and circulation pathways (see Häring et al. [2008] for details of the stimulation). Approximately 13,500 seismic events were detected during the six-day stimulation period (Dyer et al., 2010). A magnitude M_L 2.6 earthquake on 8 December 2006 then exceeded the safety threshold for continued stimulation. The injection was stopped ("shut-in"), and the operators opened the well to release fluid pressure in the stimulated volume ("bleed-off"). This measure did not, however, prevent the occurrence of a locally felt M_L 3.4 earthquake some 5 h after the shut-in. The seismicity decayed rapidly following the bleed-off (Häring et al., 2008; Deichmann and Giardini, 2009), and the project was stopped in 2007 following a detailed risk study.

Numerous studies have discussed various properties of induced (micro)seismicity, and the interactions between the evolving pore pressure field and the seismicity. These have included investigations into spatiotemporal seismicity patterns (Häring et al., 2008; Deichmann and Giardini, 2009) and earthquake source parameters (Deichmann and Ernst, 2009; Goertz-Allmann and Wiemer, 2013; Kraft and Deichmann, 2014), time- and space-dependent behavior of stress drops and the b value (Bachmann et al., 2012; Goertz-Allmann et al., 2011), the triggering role of the fluid pressure front (Terakawa et al., 2012), and the associated stress redistribution (Catalli et al., 2013). Seismicity data have also been used in the context of hazard assessment (Shapiro et al., 2007) and probability-based monitoring (Bachmann et al., 2011), which targets the real-time evaluation of seismicity evolution for potential injection tuning, to control the induced ground shaking. These tools can image and monitor reservoir properties with high resolution as long as seismicity data can be analyzed. Here, we demonstrate that analysis of seismic noise records offers the possibility to study aseismic responses associated with the stimulation. The applied passive methods help to track and image a transient that begins with the onset of the stimulation and continues for days after the induced seismicity rates are significantly reduced. Deformation is mainly resolved in the sedimentary layer above the stimulated volume that is situated in the crystalline bedrock. We invert the time-dependent relative velocity change and waveform decorrelation data (loss of coherence) to estimate the spatial distribution of the induced perturbation relative to the preinjection reference state. The results indicate that there was subsidence of the material above the stimulated volume. Our study implies that noise-based techniques constitute relevant complementary tools for reservoir monitoring, by providing continuous observables during seismically quiet periods.

DATA

We analyze one year of vertical component data (early August 2006 to mid-July 2007) that were recorded prior to, during, and after the 2006 Basel reservoir stimulation. We use the continuous noise records from five borehole stations (equipped with velocity geophones) and five surface stations (with accelerometers) that are distributed around the injection site, within a radius of approximately 5 km (Figure 2a). We focus on those accelerometers that are characterized by a high dynamic range and that had been continuously collecting data. Short-period borehole Galperin velocity geophones (4.5 Hz natural frequency) were installed between 317 and 1213-m depth (Figure 2b). The injection hole was drilled into the crystalline basement to a depth of 4700 m. Hence, the borehole sensors were located above the injection and above the boundary between the sedimentary and basement layers, which is at approximately 2500-m depth (Häring et al., 2008; Deichmann and Giardini, 2009). We compute the Rayleigh-wave sensitivity functions (Herrmann, 2006) to estimate the vertical resolution of our frequency-dependent analysis. We use the local velocity model of Deichmann and Ernst (2009). The sensitivity in the microseisms' frequency range (0.1–0.4 Hz) was confirmed using a regional model with poor resolution near the surface, but with better resolution below 3-km depth (Husen et al., 2011), noting that *microseisms* refers to large-amplitude noise excited by nonlinear ocean-wave interactions with the solid earth, in contrast to *microseismicity*, which means small earthquakes. The vertical motion for the borehole sensors was obtained from the three components oriented in the Galperin sensor configuration. This transformation is insensitive to the unknown horizontal orientation of the downhole sensors. The vertical component data from the surface Kinematics EpiSensor accelerometers were integrated to obtain the velocity seismograms. We remove the instrument response and decimate all time series using a 50-Hz sampling rate.

ANALYSIS OF VELOCITY EVOLUTION AND WAVEFORM COHERENCE

Preface

A general challenge in noise-based monitoring approaches is the separation of robust observations associated with medium changes from spurious measurements caused by variations in the excitation pattern (Colombi et al., 2014). Different filtering strategies have been applied to suppress fluctuations and to mute the biasing of wavefield components (Baig et al., 2009; Stehly et al., 2011), although their application has not become standard. Although it is common to study frequency-dependent and lapse-time-dependent trends, most analysts use only one of the two frequently used velocity-change estimation techniques (here, lapse time refers to the time along the seismogram). By applying both techniques for different frequency bands and lapse-time windows, together with filtering, multiple averaging, and smoothing approaches, here we use a more extended range of methods and consistency checks compared with conventional monitoring studies. We thus draw from combinations of the following analysis techniques and processing parameters: two time-domain normalization approaches of original seismograms (threshold and one-bit clipping), two different reference stack periods (one year/all data or prestimulation only), four substack window lengths (from 1 to 21 days), seven frequency bands (from 0.1 to 8 Hz), application of curvelet filtering, different coda lapse-time windows (from 8 to 26 s), and two analysis methods (the stretching and doublet techniques). These efforts are necessary to ensure that the velocity change and the waveform decoherence signals obtained are caused by changes in the and scattering rock properties.

Methods

The quality of noise crosscorrelation functions depends on the data processing choices. Noise preprocessing aims to make wave-

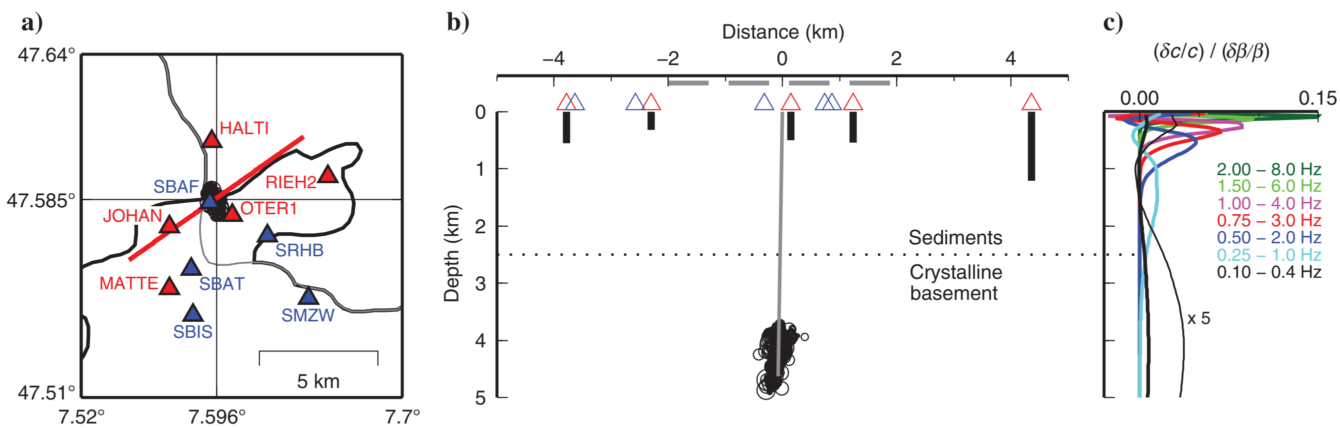

Figure 2. (a) Map of the network, consisting of five surface (blue) and five borehole (red) stations. The grid marks the surface location of the injection hole. The black and gray lines represent borders and the river Rhine, respectively; the black circles beneath SBAF are the hypocenters of induced earthquakes; and the 10-km-long red line denotes the abscissa in panel (b). (b) Cross section along the line shown in panel (a). The black circles show the earthquake locations from the catalog of Kraft and Deichmann (2014), which includes origin times between 2 December 2006, and 30 November 2007; the gray dashed horizontal line represents the approximate dimension and location of the strongest medium change (from Figure 10). (c) Frequency-dependent Rayleigh surface-wave sensitivity to velocity perturbations constitute a proxy for depth resolution. The thin black line exaggerates the thick black line by a factor of five.

field properties more compatible with the characteristics of the theoretically ideal situation of a broadband, equipartitioned state from which estimates of the Green's function can be constructed. Practitioners homogenize the frequency content of the ambient seismic wavefield and attenuate the influence of source-related transients using a range of frequency- and time-domain normalizations (e.g., Bensen et al., 2007). Our preprocessing chain has been applied previously in a variety of imaging and monitoring contexts (Poli et al., 2012; Boué et al., 2013; Hillers et al., 2014, 2015b). The daily seismograms were initially high-pass filtered and then split into six 4-h-long segments. The segments characterized by large-amplitude transients were removed. We then apply spectral whitening over a broad frequency range (20 s–20 Hz), and test the effects of two amplitude normalization approaches: threshold clipping at three times the standard deviation of the amplitude distribution in each segment and sign-keeping one-bit clipping. Crosscorrelation was performed pairwise for the stations, for each of the six segments. The correlation functions were scaled by an estimate of the total power, and they were stacked for daily Green's function estimates (Figure 3a).

Velocity-change estimates were performed for seven frequency bands $f_{\text{low}} - f_{\text{high}}$, with $f_{\text{low}} = [0.1, 0.25, 0.5, 0.75, 1, 1.5, 2]$ Hz and $f_{\text{high}} = 4 \times f_{\text{low}}$. This range over almost two orders of magnitude included low-frequency microseisms, as well as high-frequency anthropogenic noise. The noise analyzed was therefore excited by very different mechanisms. Although imaging applications use narrowband correlations for surface-wave dispersion measurements, monitoring techniques benefit from broadband signals. The factor of four accounts for the trade-off between the measurement stability and the resolution of the frequency-dependent response. Coherent energy accumulates at a rate that is proportional to the square root of the length of the correlated time series (Larose et al., 2007). In addition to the two different time-domain normalization techniques, the width of a substack window therefore constitutes another parameter in the control of the signal-to-noise ratio for any given datum. We consider substacks that consisted of averages over 1, 5, 11, and 21 daily correlation functions.

We measured the relative velocity changes using the time domain "stretching" technique (Lobkis and Weaver, 2003; Sens-Schönfelder and Wegler, 2006a) and the frequency domain "doublet" (Poupinet et al., 1984) or "moving window cross-spectral" technique (Brenguier et al., 2008a, 2008b; Clarke et al., 2011). These methods perform differently in the presence of possible wavefield fluctuations (Hadziioannou et al., 2009; Zhan et al., 2013). For the stretching method, coda waveforms at each datum are dilated by a negative or positive factor ε that optimizes the similarity of the distorted waveform to the reference signal. This factor is directly proportional to the relative velocity change $\varepsilon = dv/v = -dt/t$, where dt/t denotes the relative traveltime change. The similarity was quantified by the correlation coefficient cc associated with the optimally dilated waveform (Wegler et al., 2009). Waveform similarity was also assessed during the two-step regression analysis that comprised the doublet technique (Clarke et al., 2011), although the resulting averages were associated with the original waveforms, and were thus consistently lower compared with the stretching-cc counterparts.

Perturbations in scattering properties associated with structural medium changes induce waveform decorrelation, which is denoted as dc (Baisch and Bokelmann, 2001; Larose et al., 2010). Here, dc is the difference between the cc_{test} value associated with a current or test ε data and an average or reference cc_{ref} estimate of the unperturbed state:

$$dc = cc_{\text{ref}} - cc_{\text{test}}. \tag{1}$$

Medium changes at different scales affect the combined estimates of ε and cc differently. In the absence of noise-source fluctuations, homogeneous ε and constant cc estimates ($dc = 0$) reflect similar homogeneous variations in the velocity structure on scales exceeding the halo of the scattered correlation coda wavefield (Brenguier et al., 2008a; Hillers et al., 2014). The other extreme case is characterized by localized defects at even subwavelength scales that cause a dc signal by altering the scattering paths (Michaels and Michaels, 2005; Larose et al., 2010; Rossetto et al., 2011; Planès et al., 2014, 2015), but do not delay the propagation, and will thus leave velocity change estimates unaffected. The coda wave-based dc method is more sensitive and more general compared with phase-shift methods for the detection of small changes. In between these two end-member cases, there are the presently discussed results: spatially variable ε estimates observed together with more or less strong dc episodes indicate medium changes that are characterized by variations in the elastic properties and by structural changes on scales smaller than the network size (Hobiger et al., 2012; Obermann et al., 2013a). For the stretching method, this means that an optimal dilation of the test waveform (i.e., matching the velocity

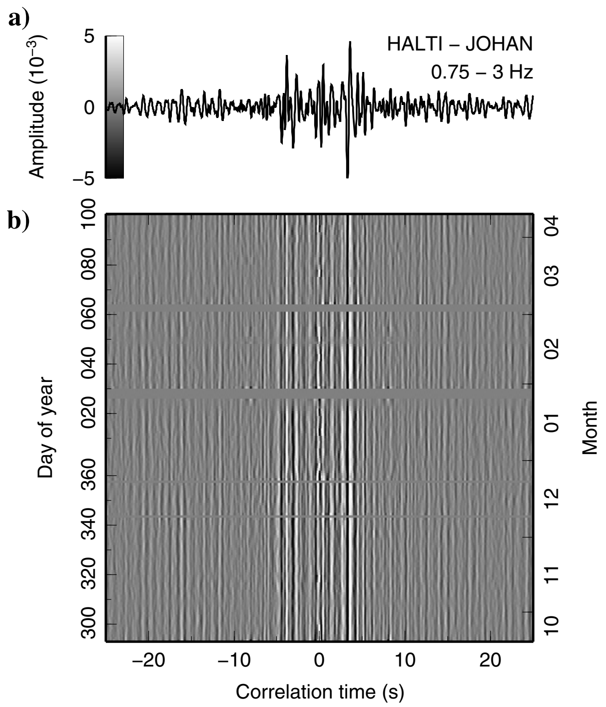

Figure 3. (a) Reference correlation for the station pair HALTI-JOHAN in the frequency range from 0.75 to 3.0 Hz, showing the stack of daily correlations from the prestimulation period. Small amplitude values are the result of band-pass filtering of a broadband correlation function. (b) Temporal pattern of the correlation function showing good coherence of coda arrivals later than 20 s. The waveform at each datum consists of correlations stacked over five days. The gray scale corresponds to the amplitude scale in panel (a).

change) cannot account for the residual dc (i.e., induced by changes in the scattering structure).

The lapse time τ range for which scattered coda waves have sufficient energy can be estimated from the decay behavior of the average correlation coda envelope, as assessed on a logarithmic scale (Hillers et al., 2015b). Arrivals with energy above an asymptotic background level are associated with strong multiple scattered phases, in contrast to the relatively incoherent noise that dominates the waveforms in the tail. We find that the transition occurs approximately at 40 s (30 s) for 0.5–2 Hz (2–8 Hz) filtered correlations. The velocity change analysis was performed in 10-s-long coda time windows between the maximum moveout surface wave arrival and the asymptotic transition (Figure 3). Note that the longest period in each frequency band controls the size of the overlapping moving windows in each analysis window. The 0.1–0.4 Hz analysis is therefore on the edge of feasibility. Analysis of lapse-time-dependent velocity changes and decoherence behavior can yield crucial information to assess the governing associated mechanisms: wavefield fluctuations biasing small-τ estimates tend to decrease rapidly, and signals observed at larger τ can be associated with medium changes (Colombi et al., 2014).

Results

Seasonal response

We reiterate that comparison of data from a large parameter space allows us to separate the universal, and thus medium, change-related signals that are independent of processing details from fluctuations that are governed by source-related wavefield changes that can be suppressed by tuning. To assess the system response to environmental changes, we begin by analyzing the dv/v and dc seasonal variations using all of the data (August 2006 to July 2007) for the reference stack. Figure 4 shows the smoothed network-average low-frequency (0.1–0.4 Hz) and high-frequency (0.5–2 Hz) energy recorded for the vertical channel, as a proxy for source variability (Figure 4a), the annual rainfall records (Figure 4b), the results of an "all-stack" (Figure 4c), and the average cc, dv/v, and dv/v error estimates in the low- and high-frequency regimes (Figure 4d and 4e) obtained with 11-day-long substacks, i.e., averaging over ±5 days around the current date. The estimation of the daily energy followed Hillers et al. (2012a). For the modeled low-frequency energy, we use a microseisms excitation database (Hillers et al., 2012b), and we attenuate global source-strength estimates to the observation site, assuming surface-wave propagation. The general trends in the observed and modeled microseisms, energies are similar, and the differences appear to be controlled by the missing coastal interactions in the model and the neglect of the excitation in the Mediterranean. For the all-stack, we stack the cc time series obtained in the seven frequency bands between 0.1 and 8 Hz, and in the two lapse-time windows (8–18 s and 16–26 s). Importantly, we did not substack the daily correlation functions for this all-stack, to limit the contamination associated with intermittent acquisition problems that potentially escaped our data quality measures. Prior to averaging over all of the 45×14 cc records obtained with the stretching and doublet method, we remove the mean from each time series. The average velocity-change errors were computed using the estimates of Weaver et al. (2011) and Clarke et al. (2011) for the stretching and the doublet results, respectively.

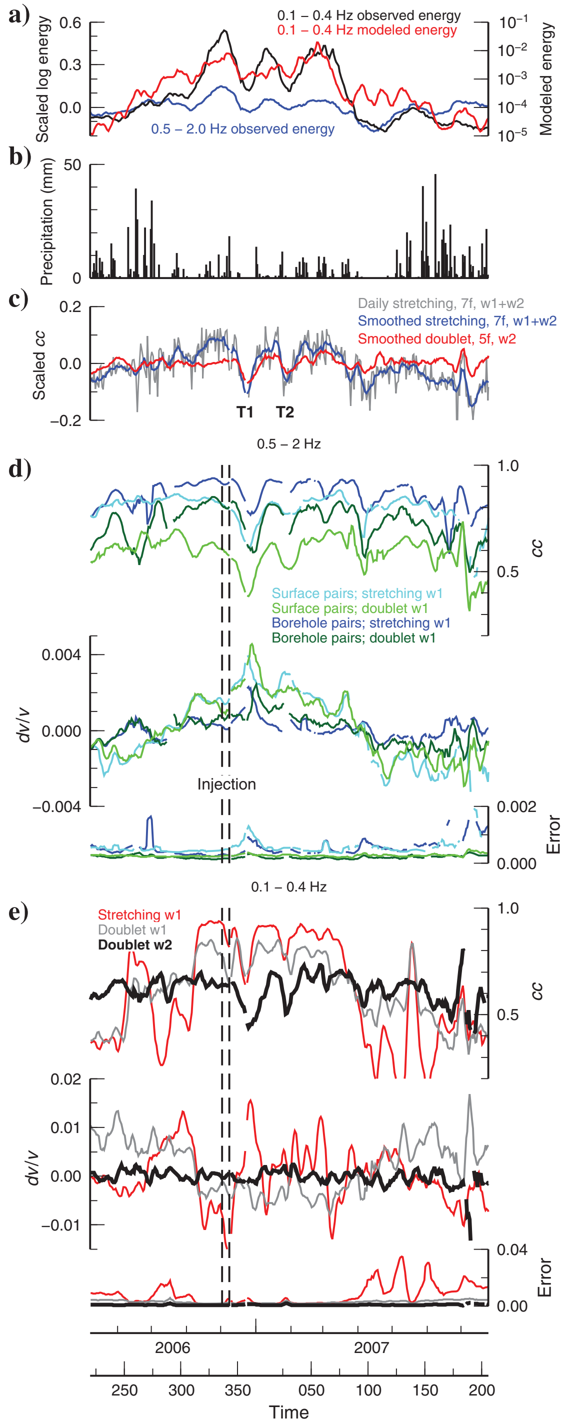

Figure 4. (a) Observed and modeled energy. The daily estimates were smoothed with an 11-day running average to emphasize long-term trends. (b) Precipitation measured in Basel. (c) Scaled decorrelation from all-stacks. The terms 7f and 5f refer to using seven (all) and the five high-frequency bands, respectively. (d) Correlation coda waveform similarity (cc), relative velocity-change estimates (dv/v), and average-dv/v error estimates obtained in the 0.5- to 2-Hz frequency range. The errors for the stretching and doublet method were calculated following Weaver et al. (2011) and Clarke et al. (2011), respectively. We use substacks of 11 days. Colors indicate different network subsets and analysis techniques. (e) As for panel (d), for the 0.1–0.4 Hz range using all station pairs. In panels (c-e), w1 and w2 refer to the lapse-time windows of 8–18 s, and 16–26 s, respectively.

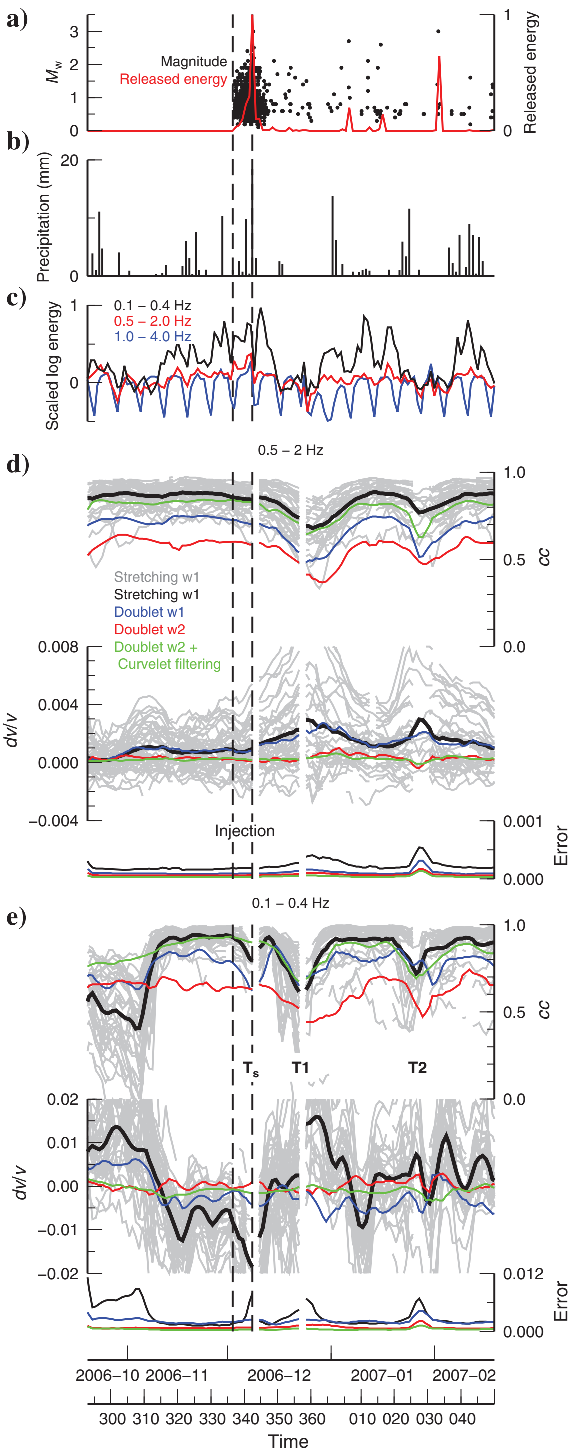

Figure 5. Focus on the time period around the reservoir stimulation. (a) Seismicity (Kraft and Deichmann [2014] M_w scale is different from the M_L magnitudes discussed in the main text) and daily released energy (linear scale). (b) Rainfall. (c) Daily network average noise energy estimates. Gray lines in panels (d and e) indicate estimates associated with individual station pairs. The black, blue, and red lines are averages. The same conventions apply as in Figure 4d and 4e. The terms T_s, T1, and T2 indicate transients.

The strongest signal in the velocity-change estimates is the seasonality in the waveform similarity cc in the microseisms frequency band (0.1–0.4 Hz; Figure 4e). The signal quality is highest during the northern hemisphere winter months (compare with Figure 4a), and it degrades significantly when the excitation pattern shifts to the southern hemisphere. This effect is strongest for the stretching result for both of the lapse-time windows considered (Figure 4e, red and gray lines; w1: 8–18 s and w2: 16–26 s). The source-dependent seasonality and intermittent fluctuations are less strong in the doublet results (Figure 4e, black lines), which indicates that this technique is less sensitive to systematic amplitude fluctuations (Zhan et al., 2013). Because the seasonal signal is inconsistent across the stretching and doublet results obtained for the different lapse-time windows, this feature has to be considered a spurious measurement, in particular contrast to the decorrelation transients around the turn of the year 2006–2007. We consider the velocity-change estimates obtained with the stretching method in the microseisms band to have little validity.

The high-frequency waveform coherence (0.5–2 Hz) shows no consistent annual trend (Figure 4d). This suggests that the associated seasonal velocity change is genuine. The good agreement between the stretching and the doublet results — even at early lapse times — is another indicator that these results are controlled by changes in the elastic medium properties. These changes are likely to be controlled by the variable water content at shallow depths (Sens-Schönfelder and Wegler, 2006a) because the velocities are low at times of high rainfall activity and because the signal is strongest at the surface stations. All of the velocity-change and similarity time series shown were obtained with the threshold-clipping approach. The results based on one-bit clipped seismograms are very consistent, but they are generally characterized by cc values that are on average approximately 0.1 points lower.

Short-term fluctuations characterize the low- and high-frequency responses. Some of these are governed by changes in the excitation pattern, most notably at low frequencies. Again, a good indicator of a governing medium change is consistency between stretching and doublet results, and results obtained at various frequencies and lapse times. Above all, the late lapse time cc results obtained with the doublet technique (Figure 4e, black lines) convince us that the decorrelation transients around the turn of the year are governed by changes in the propagation medium. The associated network average dv/v time series shows no signal, but the broadening of the daily dv/v-value histograms around the neutral mean (not shown) indicates changes in the velocity structure. The same decorrelation transients also occur at higher frequencies (Figures 4d, 5d, and 6a), i.e., for frequency bands associated with different noise-excitation mechanisms. This consistency implies governing medium effects, considering that simultaneous source effects across a wide frequency range are unlikely. At 0.5–2 Hz, the larger first transient T1 at the end of 2006 is also evident in the average velocity-change records. Further evidence that transient T1 was actually governed by changes in the medium is provided by the cc all-stack, which amplifies universal variations and mutes spurious fluctuations. Figure 4c emphasizes, convincingly we believe, the universality of T1. It can be enhanced by limiting the all-stack analysis to late lapse times only (Figure 4c, red line). The omission of the low-frequency contributions in the w2 window stack (16–26 s) illustrates the frequency-dependent seasonal trend discussed above.

The transient

In the following, we focus on the relation of T1 to the reservoir stimulation and we provide further evidence that this signal reflects an aseismic response. In Figure 5, we show the properties of induced seismicity (Figure 5a), rainfall records (Figure 5b), and high- and low-frequency energy estimates (Figure 5c). Using 11-day substack data, the gray lines in Figure 5d an 5e represent the cc and dv/v estimates associated with individual station pairs (stretching technique, 8–18 s), the black line is the corresponding average, and the blue and red lines indicate the averages obtained with the doublet method in the 8–18 s and 16–26 s windows, respectively. Figure 6 provides similar data for another pair of low- (0.25–1 Hz) and high-frequency (1–4 Hz) observations. As before, the consistency obtained with the different techniques and the different lapse times supports the interpretation that T1, and similarly T2, at the end of January 2007, were governed by transient medium changes. The low-frequency cc results also support this conclusion (Figure 5e) because the consistent features across all of the processing parameters are the decorrelation episodes T1 and T2. The early window results show a spurious transient T_s during the injection period. It seems obvious to associate T_s with seismicity-induced medium changes, considering the coincidence with the released energy (Figure 5a) and the depth sensitivity of microseisms surface waves (Figure 2c). However, T_s does not persist at later lapse times, and it is therefore unlikely to be controlled by changes in scattering properties.

The rainfall pattern does not correlate with the dv/v and cc values obtained for transient-related time scales (Figure 5b), which is similar to other environmental records (e.g., temperature, pressure, and wind speed) that are not shown. In contrast, the noise amplitudes varied on the time scales of interest here (Figure 5c). This might be an indicator of nonstationary wavefield properties that can complicate correlation coda-based monitoring, due to variable signal-to-noise ratios (Hillers et al., 2012a). Curvelet denoising filtering (Stehly et al., 2011) removes transient source-related effects that are short relative to, say, seasonal trends. In addition to the all-stack analysis, the evidence in support of a physical medium change thus includes the persistence of the T1 decorrelation episode after application of the curvelet filtering (Figure 5d and 5e, green lines). This, too, indicates that the waveform decoherence is governed by changes in the scattering properties, and it is not an artifact controlled by noise-source fluctuations. The similarity between the green and red lines in Figure 5d and 5e illustrates the concept that scattering acts as a natural source-effect filter. Here, too, daily dv/v histograms (not shown) indicate more variable pair-dependent velocity change estimates than indicated by the almost neutral green and red averages.

The individual high-frequency dv/v estimates (Figures 5d and 6a, gray lines) also indicate that the response is more heterogeneous compared with the mean. The velocity change depends strongly on the station pair, and it even varies in sign. This implies a spatially variable medium change on scales smaller than the network size, a concept that will be quantified by the spatial distributions that are discussed below, and that explains the reduced average amplitudes at later lapse times. Again, the high level of fluctuations in the low-frequency stretching estimates inhibits the corresponding inversion, although the cleaner doublet data imply a spatially variable pattern. Note that the sparse seismicity after the shut-in occurred at depths associated with the stimulated reservoir (Figure 2b). This means that the processes in the sedimentary layer that are resolved with frequencies >0.5 Hz were aseismic.

The remainder of this study focuses on an investigation of the largest transient, T1, that followed the water injection. The choice of the reference period can be an important tuning parameter (Sens-Schönfelder et al., 2014). To highlight persistent medium changes, we change the reference stack period from 1 year to 40 days

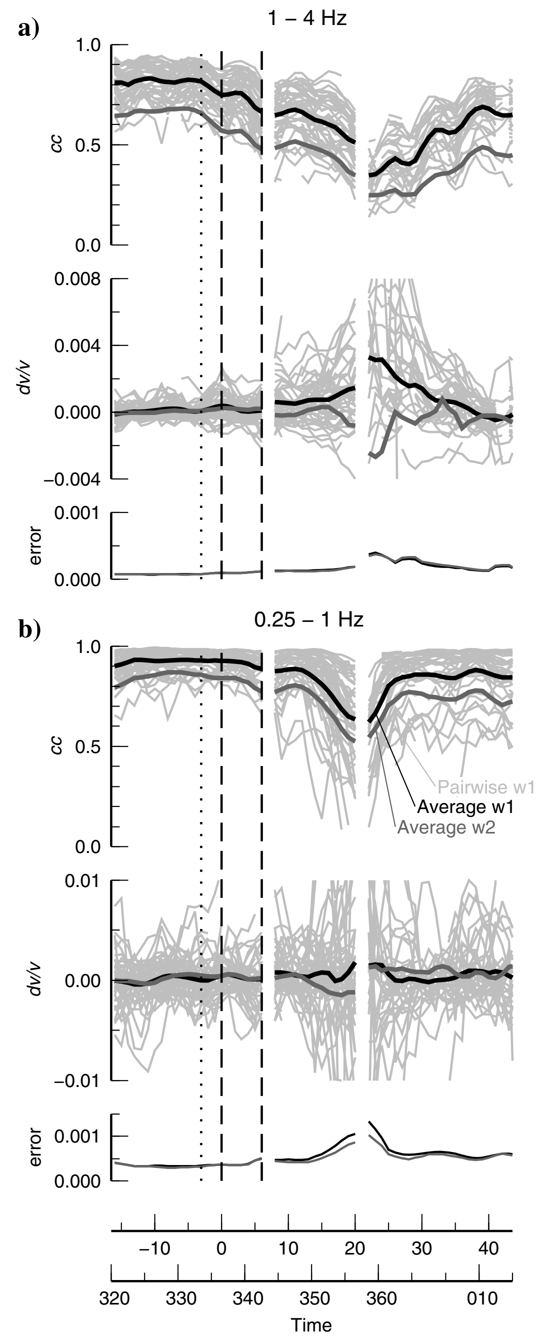

Figure 6. Focus on transient T1. The same conventions apply as in Figures 5, 4d, and 4e, respectively. Here we used the stretching method, a prestimulation stack and a substack window of five days. The vertical dotted line indicates the substack limit associated with correlations at the day of the injection start. Light gray data were used in the inversions.

before the stimulation episode. A short substack window of five days leaves a weekly periodicity in the high-frequency waveform similarity at early lapse times (Figure 6a) that decreases with τ. This trend can be observed for frequency bands above 1 Hz. The amplitude of the seven-day *cc* fluctuations is significantly smaller compared with the T1 decorrelation signal. A portion of the T1 signal coincides with the Christmas vacation in the Basel canton, although the vacation time does not perfectly coincide with the decrease in the average energy >1 Hz. The decrease in the high-frequency energy during this vacation is also lower compared with the weekly variations (Figure 5c). From this and other indicators, and notably from the inconsistency during 2007 vacation episodes and the all-stack decorrelation signals, we conclude that the vacation pattern is not controlling the experiment. The consistent frequency-dependent offset between the pretransient and posttransient *cc* levels further indicates a permanent medium change, and this offset is incompatible with a transient two-week excitation change. To summarize, the anthropogenic excitation rhythm affects the signal-to-noise ratio of our measurements, but it does not challenge the general conclusions regarding the governing medium changes.

Amplitude estimates (Figure 5c) are indicative of frequency-dependent wavefield fluctuations, although they do not conclusively relate to the stability of the wavefield composition (Hennino et al., 2001). We estimate the propagation directions for the reference and the 15-day peak T1 period as an additional wavefield marker. We compute estimates of the azimuthal noise intensity B (Stehly et al., 2006; Larose et al., 2007; Weaver et al., 2009; Froment et al., 2010) from crosscorrelation functions, as described by Hillers et al. (2013), to determine whether systematic B changes correlated with the *cc* or dv/v signals, which would indicate potential bias (Colombi et al., 2014). Instead, the essentially identical patterns for the reference period and the T1 period (Figure 7) for all of the frequency bands are an additional indicator that our measurements are not systematically controlled by variations in the noise properties. The timing and duration of the T1 signal with respect to seismic activity (Figure 5a) ruled out systematic bias in our measurements through earthquake signals. Even at high frequencies (1–10 Hz), the correlation functions were insensitive to the intermittent wavefield changes associated with the seismicity pattern.

Together, these observations imply that the signals obtained are governed by changes in the medium. Again, the strongest argument comes from the consistency of the observations made with the many different analyses. We can conclude that the potentially stimulation-

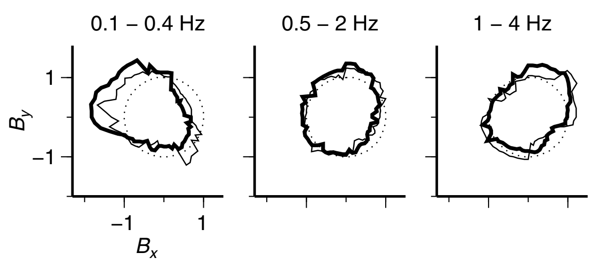

Figure 7. Frequency-dependent distribution of scaled noise intensity $B(\theta)$. The thick line corresponds to the prestimulation reference period, the thin line to a 15-day period that covered transient T1, and the dotted line to the average $B(\theta) = 1$. At 0.1–0.4 Hz, the above-average values in the northwest quadrant correspond to microseisms excitation in the north Atlantic (Koch and Stammler, 2003; Hillers et al., 2012b).

triggered transient T1 is not controlled by systematic wavefield fluctuations, although variable excitation can affect the resolution of some of its properties. To further investigate the nature of the transient response, we constrain the spatial extent of the perturbation. A first evaluation of the vertical resolution can be obtained from the T1-related velocity changes that affected the correlations from the surface-surface, surface-borehole, and borehole-borehole station pairs. This is different to the response to the assumed variable water content at shallow depths (Figure 4), which mostly affected measurements from the surface-surface station pairs, in contrast to correlation functions constructed from downhole stations. The changing groundwater level cannot be resolved with measurements at depth, which indicates that these changes were not large enough (Hillers et al., 2014). This difference in the sensitivity between T1-related and water-level changes implies that variations in physical properties associated with the reservoir stimulation occurred in an extended vertical region.

Frequency and lapse-time dependence

The systematic frequency and lapse-time dependence of the velocity change and decorrelation signals (Figures 6 and 8) are related to the location and size of the causative medium change. As detailed below, the sensitivity to medium changes of the correlation coda wavefield in the considered lapse-time range is dominated by the properties of surface waves. Hence, frequency constitutes a first-order proxy for depth, considering the Rayleigh-wave sensitivities (Figure 2c). As discussed, the fluctuations in the low-frequency wavefield did not allow robust velocity-change estimates at 0.1–0.4 Hz. Relatively stable measurements could be made at frequencies greater than 0.25 Hz. The largest dv/v changes are obtained with the three bands between 0.5 and 4 Hz, which indicates that the consistent velocity variations at depths around and below 500 m were larger compared with the variations in the top 200 m. The network average decorrelation pattern is similarly frequency dependent. The two low-frequency responses (0.1–0.4 Hz and 0.25–1 Hz) are characterized by an overall shorter transient duration and faster recovery, compared with the high-frequency results (e.g., the *cc* data in Figure 6). We estimate the relative timing of the peak decorrelation between the different frequency bands. The resulting distributions of the station pairwise differential peak times are an additional indicator that we resolve processes at depth. The peaks of the five highest frequency bands coincide, and the 0.25–1 Hz peak occurs some 3–5 days earlier. The 0.1–0.4 Hz decorrelation peak occurs another 3–5 days earlier, although this inference is less consistent over the range of tested techniques, lapse times, and smoothing windows, compared with the other estimates. These results imply an upward-propagating perturbation.

We now address two aspects of τ-dependent wavefield changes for the correct taxonomy of the dv/v lapse-time changes (Figure 8). Both aspects relate to partitioning. The concept of equipartitioning implies stabilization of the deformation energy ratio of S- and P-wave components (e.g., Hennino et al., 2001). This is a lapse-time independent signature of the medium and it emerges once the propagation has entered the diffusive regime. Equipartition markers (Hennino et al., 2001; Paul et al., 2005; Margerin et al., 2009) can be used as proxies for relevant changes in wavefield properties. In contrast to equipartitioning, there is what can be referred to as the partitioning of sensitivity. For the common situation of the source and receiver located at the surface, the scattered phases that arrive after the direct surface wave are also governed by waves that propagate along the surface. The probability that an arrival has sampled deeper parts (as a body wave) increases with τ (Obermann et al., 2013b). The rate at which this process occurs is controlled by scattering and wave conversion, and hence, by medium heterogeneity. As a consequence, the sensitivity to medium changes near the surface and at depth decreases and increases with τ, respectively. For the vertical-vertical correlation component, Obermann et al. (2013b) show that the sensitivity of surface and body waves is equally partitioned at approximately six times the transport mean free time t^* — a measure of the average propagation time after which the memory of the original beam direction is lost.

We observe two lapse-time-dependent trends. The first one is the above-discussed seven-day periodicity, which vanishes at longer lapse times because the scattering progressively reduces the noise-source signature. Second, the average amplitude of the T1 velocity variation decreases with the increasing lapse time (Figure 8), toward neutral values; this effect is strongest for the three frequency bands in the 0.5–4 Hz range. The correlation coda wavefield is governed by surface waves, considering that even large lapse times are small compared with the empirical $6t^*$. Together, this implies a laterally heterogeneous velocity-change pattern. The later-arriving waves tend to average over positive, neutral, and negative regions, leading thus to the observed decrease in average (absolute) dv/v amplitude. Although the average cc level also decreases (Figures 6 and 8), the loss in coherence is less sensitive to τ, and remains significant even for late lapse times. Decorrelation is cumulative.

The detection and resolution power in general, and the lapse-time pattern in particular, depend on the potentially frequency-dependent relation between the size scale of the spatial variations, seismic wavelength, and scattering length scales (Planès et al., 2015). Estimates of t^* are equal to ℓ^*/c, where ℓ^* is the transport mean free path, and c is the wave speed. The transport and scattering mean free paths ℓ^* and ℓ are equal for isotropic scattering, otherwise ℓ^* is expected to be larger than ℓ. Average scattering length scales for the continental crust are typically of the order of tens to hundreds of kilometers (Sato et al., 2012). Lacombe et al. (2003) report $\ell^* \approx 250$ km in central France at 3 Hz, and for Germany, Sens-Schönfelder and Wegler (2006b) estimate $\ell \approx 690$ km, also at 3 Hz. However, ℓ is likely to be smaller in the target area considering the more complex tectonic setting at the southern tip of the Rhine-Graben rift system (Kastrup et al., 2004; Häring et al., 2008). Below, we work with $\ell^* = 50 - 300$ km, which leads to $\ell^*/c > 26$ s with a Rayleigh-wave speed estimate of $c = 2$ km/s. The resulting $\tau/t^* < 6$ confirms the concept that the sensitivity in the latest lapse-time window that ends at 26 s is still governed by surface-wave properties. These considerations are certainly valid for the lower range of frequencies used. Toward the high end, coherent energy between the surface and borehole stations might mainly propagate as body waves, which in principle requires a different imaging approach compared with the concept discussed next.

SPATIAL DISTRIBUTION OF MEDIUM CHANGES

The surface-wave depth sensitivity to velocity perturbation (Figure 2c) is a proxy for the vertical resolution. Simulations based on perturbations of the velocity model can refine this first-order interpretation (Hobiger et al., 2012; Obermann et al., 2013b). Only the microseisms is sensitive to the depth region around the stimulated reservoir, and the higher frequencies resolve processes in the overlying sedimentary layer. To further study the material responses, we invert the ε and dc measurements obtained with the stretching technique to image the medium changes, although the stretching data appeared to be more sensitive to changes in the wavefield anatomy compared with the doublet technique. We adopt this procedure because only the stretching technique allows estimation of the residual decoherence between the waveforms that had been corrected for the velocity-change effect. However, we limit the inversion and interpretation to signals that had been validated with the doublet method and various other parameter combinations. We consider the 2D problem associated with the lateral propagation of the frequency-dependent surface waves. We begin here with an introduction to the approach developed by Pacheco and Snieder (2005), Larose et al. (2010), Rossetto et al. (2011), Obermann et al. (2013a, 2014), Planès et al. (2014, 2015), and we extend the assessment of the solution quality by forward tests.

Inversion approach

The velocity-change ε_i and decoherence dc_i estimates associated with a station pair i were obtained from the analysis of the correlation coda waves that followed scattered paths between the stations. Recall that phase-delay tools detect extended variations in the elastic properties. Decorrelation is sensitive to structural changes (extended or localized) in the medium, i.e., to modifications in the scattering structure. For imaging, observations i are related to the space ele-

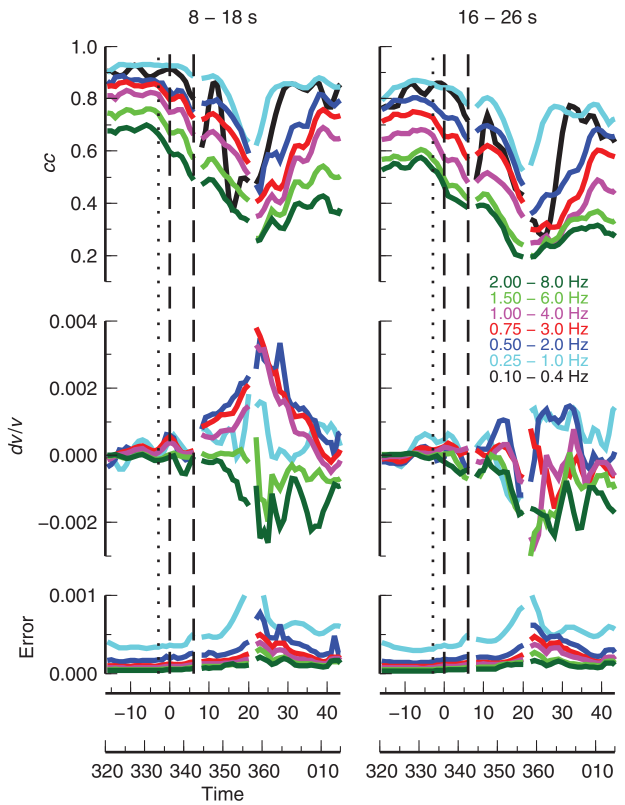

Figure 8. Average lapse-time dependence of cc, dv/v, and the error estimates for seven frequency bands. Data are as in Figure 6. Velocity change estimates for the low-frequency microseisms band 0.1–0.4 Hz (black data) are not shown because they are not reliable and they fall off scale.

ments of the medium sampled by the coda waves. Scattering prohibits the association of a specific arrival in the seismograms with a ballistic — computable — trajectory in the medium. Wave propagation is therefore described statistically (e.g., Pacheco and Snieder, 2005); i.e., the propagation is approximated by kernels that represent estimates of the spatial distribution of the residence time governed by random walks between two stations.

Kernel

The probabilistic wave propagation in the scattering regime was calculated using the solution to the radiative transfer equation (Boltzmann transport equation). For 2D isotropic scattering, the solution reads as follows (Shang and Gao, 1988; Sato, 1993; Paasschens, 1997):

$$p(r,t) = \frac{e^{-ct/\ell^*}}{2\pi r}\delta(ct-r) + \frac{1}{2\pi\ell^* ct}\left(1-\frac{r^2}{c^2t^2}\right)^{-\frac{1}{2}} \times \exp\left[\ell^{*-1}\left(\sqrt{c^2t^2-r^2}-ct\right)\right]\Theta(ct-r), \quad (2)$$

where c is the wave speed, r is the distance between the source and receiver, ℓ^* is again the transport mean free path, and $\Theta(x)$ is the Heaviside step function. The first term describes the coherent part of the intensity that decreases exponentially with the distance relative to the transport mean free path. The second term describes the diffuse intensity. The diffusion solution is reached asymptotically for $t \gg r/c$. This intensity propagator describes the probability that the wave has traveled between two points in the medium during time t. Estimates of ε_i and dc_i are then related to medium perturbations at $\mathbf{x}_0$ using the sensitivity kernel introduced by Pacheco and Snieder (2005), Larose et al. (2010), and Planès et al. (2014):

$$K(\mathbf{s}_1,\mathbf{s}_2,\mathbf{x}_0,t) = \frac{\int_0^t p(\mathbf{s}_1,\mathbf{x}_0,u)p(\mathbf{x}_0,\mathbf{s}_2,t-u)\mathrm{d}u}{p(\mathbf{s}_1,\mathbf{s}_2,t)}, \quad (3)$$

where $\mathbf{s}_1$ and $\mathbf{s}_2$ are the station positions and $t=\tau$ is the center of the coda lapse-time window over which the analysis was performed. The intensity propagator in the radiative transfer solution (equation 2) is $p(\mathbf{s}_1,\mathbf{s}_2,t)$. The kernel K represents a spatial probability distribution of the detention time around $\mathbf{x}_0$. For the computation of p (equation 2), we use $c = 2$ km/s. The scattering length scale ℓ^* is usually more difficult to estimate (Campillo, 2006). Here, we use $\ell^* = 50$ km, which is motivated by the relatively complex geologic setting (e.g., Figure 1; Deichmann and Giardini, 2009). Obermann et al. (2013a) test the sensitivity of the inversion toward different values of ℓ^* and observe that ℓ^* had an influence on the size of the affected area, but not on the location itself. Similarly, our inversion results differed very little using a range of c ($2-3$ km/s) and ℓ^* (50–300 km) values. The Ks are characterized by two peaks at the locations of the two stations. The spatial discretization can therefore influence the resolution, in particular, in the network center with subkilometer horizontal distances between the injection hole and the stations OTER1 and SBAF (Figure 2a). Small cell sizes provide more accurate solutions that are characterized by correctly resolved peaks but increase the computational costs. We find that a cell size of 0.0075° for the parameter test studies was sufficient for the resolution of the main features. For illustrative purposes, we use here a resolution of 0.0025°.

Inversion

To estimate the horizontal distribution of the changes in the study area, we formulate the forward problem using a system of linear equations in matrix form:

$$\mathbf{d} = \mathbf{G}\mathbf{m}, \quad (4)$$

where $\mathbf{d}$ is a vector for which each $d_i (i = 1\ldots n)$ corresponds to a ε_i or dc_i estimate associated with a given station pair, n is the number of contributing station pairs, $\mathbf{G}$ is a matrix for which each G_{ij} corresponds to K for station pair i in cell j weighted by the surface of a computational cell $\Delta s = (0.0025°)^2 \approx (0.28\ \text{km})^2$ and the inverse of the lapse time $1/\tau$ in the coda (velocity changes) or the Rayleigh-wave group velocity c (decoherence), and $\mathbf{m}$ is a vector for which each component m_j contains the actual relative velocity changes that we estimate for each pixel j (dimensionless) or the scattering cross-section density σ (km/km^2):

$$d_i = \varepsilon_i, \quad G_{ij} = \frac{\Delta s}{\tau}K_{ij}, \quad m_j = (dv/v)_j,$$
$$d_i = dc_i, \quad G_{ij} = \frac{c\Delta s}{2}K_{ij}, \quad m_j = \sigma_j. \quad (5)$$

When the inverted data are velocity changes, there is no constraint concerning the sign of $\mathbf{m}$. We can thus directly use the formulation of the linear least-squares method as proposed by Tarantola and Valette (1982). To estimate the standard deviation $\text{std}_{d,i}$ of the ε data, we use a theoretical estimate proposed by Weaver et al. (2011) that depends nonlinearly on signal coherence, frequency, bandwidth, and duration. For the dc_i inversion, we use $\text{std}_{d,i} = 1 - cc_{\text{ref},i}$.

Smoothing is important because the inverse problem is underdetermined in most cases. The choice of the smoothing or correlation length λ and the model variance std_m is a trade-off between the fit of the data to the model and the smoothness of the solution. Estimates are obtained from a so-called L-curve (Hansen, 1992), which describes the population of grid search solutions associated with a range of λ and std_m values in a $\mathbf{m}_{\max}$-rms space. Here, $\mathbf{m}_{\max}$ denotes the maximum fluctuation in the model distribution (dv/v or σ), and rms denotes the root-mean-square between the measured and modeled medium changes. In the dc inversion, the σ estimate obtained is necessarily positive, and we thus impose a positivity constraint. The initial model is again zero, and only the positive values are kept as an updated starting model in an iterative procedure. We limit the cycle to 10 iterations. We compute a solution in a 15- × 20-km area that was roughly centered on the location of the injection point, at 47.585°N and 7.596°E. This area is larger than the domain that is characterized by good resolution, to minimize edge effects.

Solution quality

To assess the resolution and credibility of the dv/v and σ distributions obtained, we first follow the work of Obermann et al. (2014) and Planès et al. (2014), and we discuss the properties of the resolution operator $\mathbf{R}$ before we present the results from the forward tests. Figure 9a shows a typical example of the averaging indices associated with the inversion of the peak T1 ε data. The averaging index for a cell i is defined as the sum of the coefficients R_{ij} of the line i in the resolution matrix. The resolution is generally good (approximately 1) in the area enclosed by the stations, and it becomes poorer toward the boundaries of the domain. Within these limits, the spread of the resolution can be evaluated for a specific cell. Figure 9b shows the resolution for a cell k in the center of the network marked by the white box, the kth line of the matrix $\mathbf{R}$. For a typical $\lambda = 1$–2 km, the spread extends more than 1–2 km in each direction. The properties of K govern the orientation of the peak values toward the nearest station location. Note that the inversion quality crucially depends on the application of radiative transfer. Using kernels governed by the diffusion approximation, the images obtained were unstable in response to small changes in the inversion parameters λ and std_m, and the misfit markers were significantly higher. This indicates a general incompatibility of the wave propagation with a diffusive model for the considered lapse-time range and the short distances between the sensors and potential changes.

Extending this formal approach for the resolution assessment, we compute the synthetic ε_i and dc_i estimates that were associated with defects located in the center and along the edge of the network. First, perturbations were imposed on an area that covered 3×3 cells at the location of the green square in Figure 9c. Theoretical $\mathbf{d}$ vectors were estimated using $\mathbf{G} = \gamma \mathbf{K}$, where γ is the corresponding scaling factor for velocity and structural changes (equation 5); i.e., the distribution characterized the response to a unit velocity change. We find that locations within the network boundaries are well resolved by the inverse operation, with the peak values oriented toward the nearest station. The spread is comparable with the estimate shown in Figure 9b. It should be noted that we impose a unit positive velocity change, which is different from the actual case, which is characterized by negative and positive ε_i estimates (Figures 5 and 6). Although the sign was not constrained in the dv/v inversion, the solution recovers the positive-only velocity perturbation and does not show spurious negative values. Second, an extended perturbation was located along the western edge of the network, within an area of good resolution (Figure 9d). The overall location is well preserved in the inversion results considering the expected fuzzy edges, and the solution is not falsely projected into the network center where the resolution is best. Finally, the inversion of random perturbations that represented uncorrelated fluctuations in contrast to localized medium changes that lead to coherent signals did not return a universal feature indicative of a spurious governing structure in the inverse problem.

Results

Frequency and lapse-time-dependent inversion results

We deduce the reliability of the T1 transient from the signal consistency across a wide parameter range, notably its persistence at late lapse times and after filtering. We continue to compare the early and late lapse-time inversion data from a range of frequencies, to determine the robustness of the imaged features. Recall that the wave-propagation model was adjusted for each lapse-time window using Ks constructed with the corresponding average τ value. In addition to using the five-day substack correlations, we average dc_i and ε_i over five days for each image. This mutes any potential fluctuations associated with the anthropogenic excitation pattern, and it further stabilizes the results. The resolved patterns are obviously sensitive to choices of the inversion smoothing parameters. In principle, the best solution for each image is associated with its individual set of values that corresponds to the maximum L-curve flexion. To avoid fluctuations between consecutive images associated with variable tuning parameters, we chose to use identical values of λ and std_m for all of the inversions. However, we confirm the consistency of the features for a range of parameters. We choose $\mathrm{std}_m = 0.2$ and $\mathrm{std}_m = 0.02$ for the ε and dc inversions, and $\lambda = 1$ and 1.5 km, respectively.

Figure 10 shows the dc (Figure 10a and 10b) and ε (Figure 10c and 10d) inversion results around the T1 peak for a wide range of frequencies and two lapse-time windows. The location of large-σ estimates in the network center (Figure 10a and 10b) is consistent for all frequency bands. There is the exception of the microseisms early window data. This inconsistency can be explained by instabilities in the associated stretching data (Figures 4e and 8e), which provides the data for the inversion. A lapse-time-dependent ε inver-

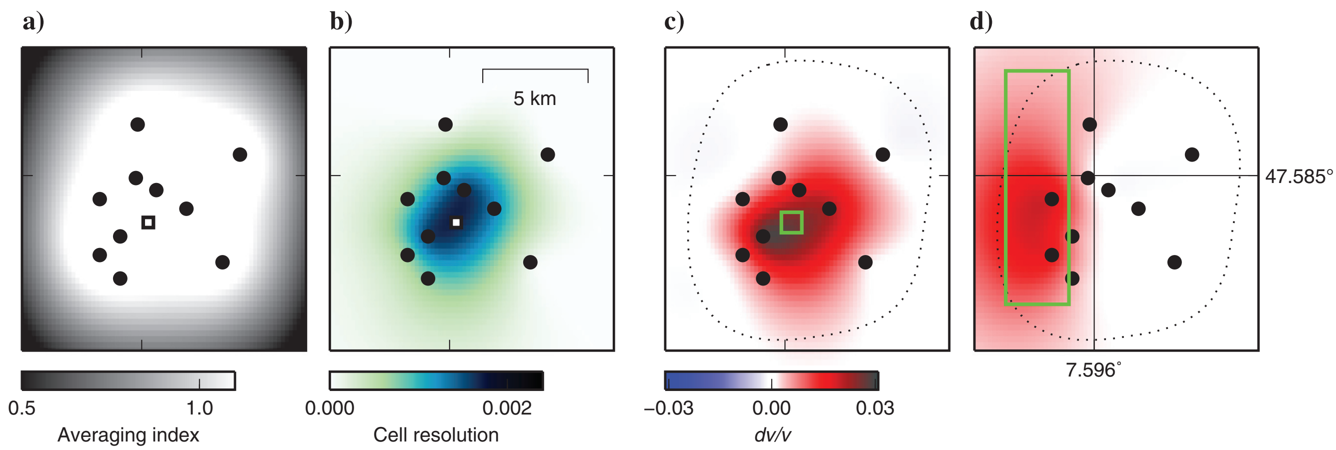

Figure 9. Resolution estimates associated with the inversions. (a) The spatial averaging index associated with the resolution matrix $\mathbf{R}$ for a cell located at the white square. The inversion was associated with 0.75- to 3-Hz, 8- to 18-s ε data around the T1 peak perturbation. (b) The spatial domain that contributes to estimates in the cell at the location of the white square. This can be tuned by the inversion parameters λ and std_m. We use values from the inversions below. (c and d) Inversions of a synthetic unit positive dv/v defect imposed over the area indicated by the green rectangles. The dotted line represents the well-resolved area using index information, as in panel (a); the black dots (in all images) show stations from which the data were used in each of the inversions.

sion returned different trends (Figure 10c and 10d). Small-τ features are consistent for all of the frequency ranges considered (the microseisms ε was not inverted because of inhibiting fluctuations). A significant, spatially confined positive velocity anomaly surrounded by areas of velocity decrease is robustly identified just south of the injection site. Later-window results confirm this observation, although the solution quality rapidly decreases due to the overall decrease in the waveform similarity. Differences between small- and large-τ results increase with frequency, which could be an indicator that the 2D wave-propagating model was inadequate.

Again, frequency is a proxy for depth. Considering the levels of the peak $(dc/c)/(d\beta/\beta)$ sensitivities (Figure 2c), the sequence of solutions indicates the stable resolution of an approximately 5-km-wide zone that is characterized by evolving damage (an increase in the scattering potential) and positive velocity changes at depths greater than 200 m in the vicinity of the injection point.

Imaging the temporal evolution

We image the temporal evolution of the transient (Figure 11). As before, we validate the discussed features using different smoothing parameters and lapse-time windows. We present the results from an early lapse-time window because of the better signal-to-noise ratio of the small-τ velocity change data. We begin with the evolution of σ (Figure 11a and 11b). The images obtained show a transient with peak values in the vicinity of the injection hole for low and high

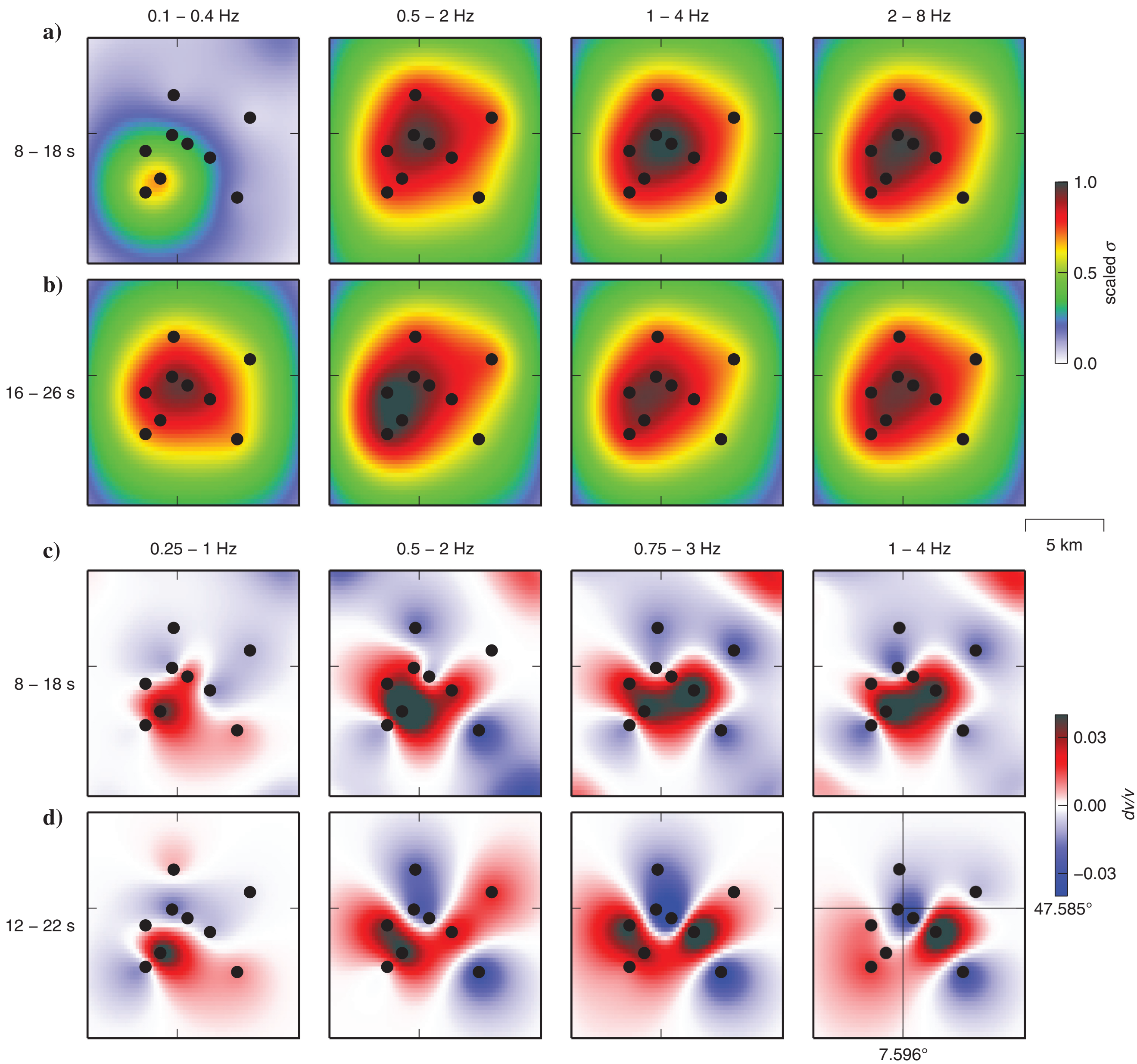

Figure 10. (a and b) Frequency and lapse-time-dependent distributions of the scattering cross-section density σ and (c and d) the relative velocity change. The color scale in panels (a and b) is adjusted to the maximum value in each image. The color scale in panels (c and d) is universal.

frequencies. The location is stable, notwithstanding the +11-day window in the microseisms band. Peak damage occurs some five days earlier in the low-frequency images, compared with the high-frequency images, which illustrates the above-discussed upward propagation. The patterns also illustrate the more rapid recovery at low frequencies, i.e., in deeper areas. The center of the σ patterns appears somewhat more north compared with the corresponding velocity-change distributions, even if the uncertainty indicated in Figure 9 is considered. These differences confirm the conjecture that decorrelation and velocity-change measurements are sensitive to different forms of medium changes. Integration of the σ distribution in the center region of Figure 11b characterized by dark colors yield an estimate of the average scattering cross section. This is a proxy for the crack size or dimension of a damaged volume (E. Larose, personal communication, 2014; Planès et al., 2014). The values obtained are relatively large and are not compatible with the volume of injected water (Obermann et al., 2013a). The results imply considerable change above the source region of the induced seismicity.

The corresponding velocity-change evolution (Figure 11c and 11d) is similarly consistent over a wide range of frequencies. Using the same smoothing parameters, the positive velocity anomaly (Figure 11c and 11d, red) that was observed at low frequencies (0.25–1 Hz) is smaller in diameter compared with its high-frequency counterpart (1–4 Hz, and higher). The windows centered on the injection period already show a small-amplitude version of this pattern, which shows progressively larger amplitudes at later times, which lends further support to a consistently resolved material response. The adopted constant parameters also imply that the imaged patterns are not controlled by variable λ or std_m choices, but follow the ε data from which they were constructed (Figures 5 and 8).

Despite the lack of data from the southernmost station SBIS (Figure 2a) in the +26-day inversion, the patterns five days earlier and later do not show different distributions, which suggests an overall robustness toward contributions from individual stations. However, the small-scale feature of the velocity decrease in Figure 11d associated with high frequencies at +1, +11, and +21 days is dominated by the OTER1 data. Negative wave-speed changes around

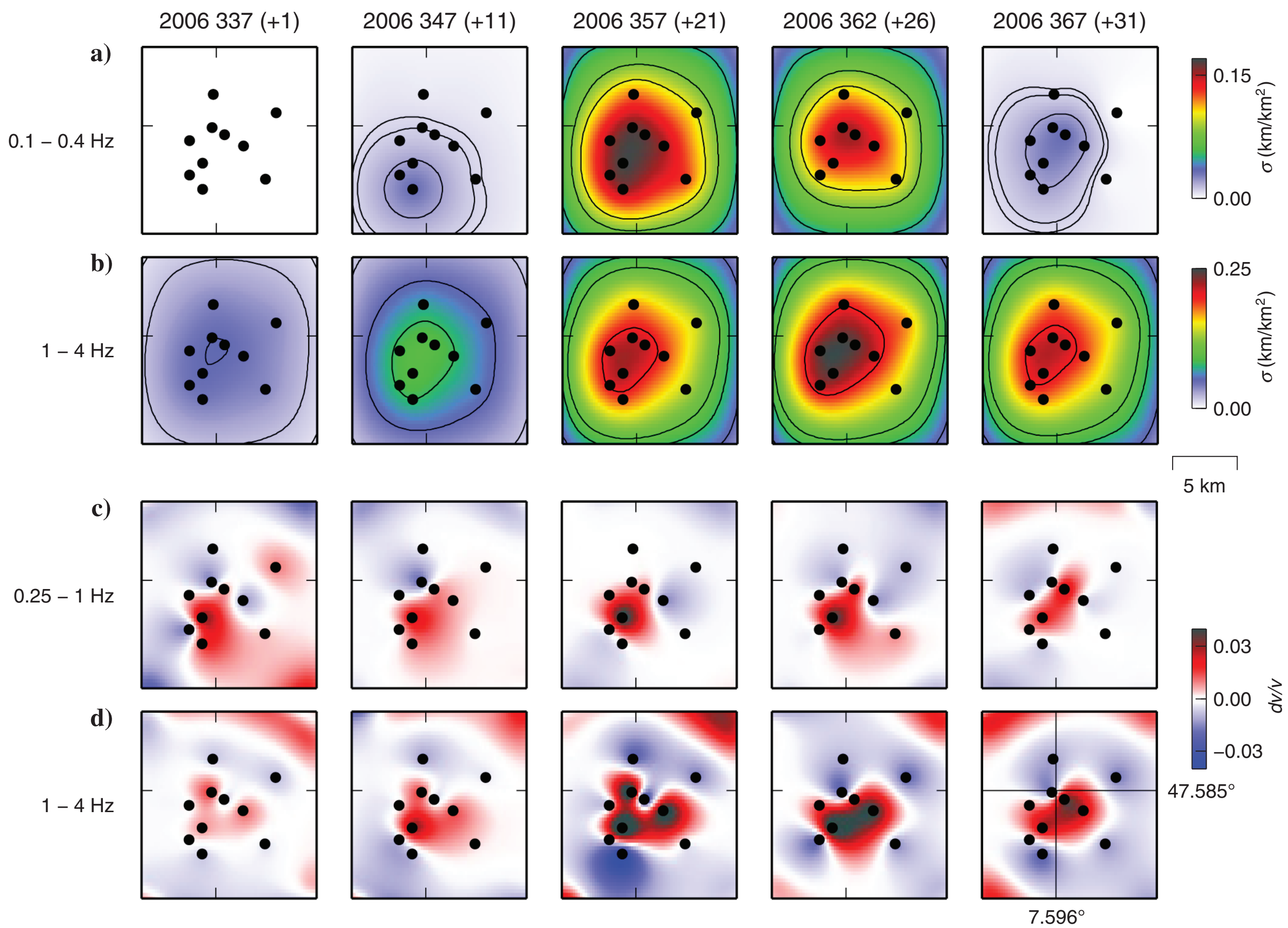

Figure 11. (a and b) Temporal evolution of σ and (c and d) dv/v patterns from low- and high-frequency data. The color scale in panels (a and b) is adjusted to the maximum in each row. The color scale in panels (c and d) is universal. The day of the year that was associated with each five-day averaging window is given at the top, together with the days elapsed since the onset of stimulation (see Figures 6 and 8). Contours in panels (a and b) aid the identification of the relative peak deformation (contours are drawn at levels 0.008, 0.01, 0.02, 0.05, 0.08, 0.1, and 0.2).

OTER1 disappear if the OTER1 data are discarded. The significance of this feature is unclear, because damping parameters do not allow resolution of scales smaller than the distance between OTER1 and SBAF (<1 km). We further test the pattern variability as a function of the station subset. Considering the mix of surface and borehole stations, we create dv/v images that consisted of the different subnetworks. All of the images show a region of increased velocities around the network center, which is surrounded by reduced wave-speed areas. The location and extension of the patterns depend on the subset and the associated resolution matrix, and they are therefore subject to some lateral uncertainty of the order of 1–2 km. However, the region that shows the strongest positive changes tends to be consistently centered south of the injection borehole. The general similarity between the solutions associated with the different subnetworks implies that the 2D radiative transfer model is reasonable, at least for the lower frequency ranges considered. There are no significant differences in the spatial distributions of the medium changes using only borehole or only surface stations. This is also consistent with the conclusion that velocity changes are not confined to the shallow subsurface. Finally, this also agrees with our previous conclusions based on frequency dependence and on the variable sensitivity to precipitation-controlled shallow water-level changes.

Conflicts with the underlying assumption that coda waves are mainly scattered surface waves can potentially occur for inversions of >1 Hz data. Reduced scattering-length scales and wave speeds can change the sensitivity of the scattered high-frequency wavefield to perturbations. However, using Ks constructed with reduced ℓ^* and cs derived from high-frequency time-distance moveout patterns did not resolve any of the early/late lapse-time dv/v ambiguities (Figure 10c and 10d, 1–4 Hz). The applied wave-propagation model might be challenged at a more fundamental level. The high-frequency propagation between the borehole and surface stations is likely to be more complicated than the horizontal propagation and scattering model used for the K construction. In this case, coherent energy sampled at depth and at the surface is scattered and multiply converted between surface- and body-wave modes, and the 2D model is likely to become inaccurate. Although kernels for the full-space 3D problem exist (Planès et al., 2014), a statistical description of this mixed situation that includes mode conversions is not available.

DISCUSSION

Our noise-based analysis of temporal variations in the material properties affected by the 2006 Basel Deep Heat Mining experiment indicates that the six-day-long reservoir stimulation triggered an aseismic deformation transient that cannot be resolved with standard microseismicity tools. The frequency and lapse-time-dependent evolution of noise crosscorrelation coda wavefield variations resolved perturbations in the scattering structure over the entire depth column (near surface to 4-km depth). The delayed occurrence of the main deformation with respect to the induced seismicity suggests that we monitor rock changes that were not immediately governed by shear or volumetric failure in the earthquake source volume. Resolution of the relative velocity changes was constrained to the overlying sedimentary layer, although the damage evolution observed with low frequencies can be mapped at least to the basement-sediment boundary. We thus resolve upward-propagating perturbations that were best resolved above the stimulated volume.

Several indicators suggest that our measurements were not spurious or biased by environmental fluctuations or by systematic changes in the anatomy of the ambient wavefield, but they were governed by genuine changes in the rock properties: (1) The robustness of the decorrelation and velocity-change signals was repeatedly verified by their consistent emergence over a large frequency range and in response to variable processing methods, analysis and filtering techniques, and averaging, smoothing, and inversion parameters; (2) we obtained signals from waveforms that were dominated by Rayleigh-waves, which have a sensitivity to perturbations down to 3–4 km in the microseisms low-frequency band; (3) coda waves of crosscorrelation functions constructed from the borehole station data resolved the perturbations; (4) this is in contrast to the sensitivity to the seasonal velocity changes that were associated with the precipitation pattern, which affected velocities near the surface, and was not resolved by the borehole data; (5) the wavefield anatomy was not influenced by the earthquake waveforms because the transient deformation peaked after the bleed-off and after the rates of induced seismicity had significantly decreased; and (6) markers of wavefield properties — average amplitude and noise propagation directions — indicated that the measurements were not biased by coherent, systematic changes in the original noise wavefield.

The first key observation obtained with our analysis is the resolution of an aseismic transient associated with upward-migrating deformation that initiated at depth with the onset of the stimulation. It is therefore likely that this was triggered by medium changes that are associated with the water injection and induced seismicity. The very detection, monitoring, and imaging of these processes emphasize the general applicability of passive methods in geotechnical and reservoir stimulation contexts, in the determination and mitigation of the potential environmental impact of unwanted responses. Prior to the here-demonstrated proof of concept to directly observe manifestations of aseismic deformation, several observations of stress variations within geothermal systems were interpreted only as indirect evidence of such phenomena (e.g., Schoenball et al., 2014).

The second key feature of interest in the context of reservoir management is the images that were obtained with the spatial inversion of the velocity-change and decorrelation estimates. The depth sensitivity of our approach was estimated from the eigenfunctions of the Rayleigh surface waves that dominated the coda wavefield at early lapse times of the vertical component noise correlations. Images constructed from these data, therefore, constitute estimates of the medium change distributions in a horizontal plane. The solutions to the 3D problem require the construction of the corresponding full-space sensitivity kernels. This approach can be feasible for (much) higher frequencies and later lapse times, when the correlation coda wavefield is dominated by body waves (Obermann et al., 2013b).

Images of the relative velocity-change distribution show a high-velocity region in the center of the network. This region is located slightly south of the surface projection of the stimulated volume indicated by the induced seismicity. The velocities are decreased in the vicinity of this approximately 5-km-wide area. This pattern is stable with respect to various processing and inversion parameters. The only variation along the transient duration is the dv/v amplitude. The regions of change in the scattering potential σ are generally colocated with the positive velocity perturbation considering the 1–2 km lateral spread. However, they appear more compatible with the lateral distribution of the induced seismicity cloud; i.e., they are centered on the injection. After the transient, the velocity-change pattern persists and the average decorrelation values show a significant frequency-dependent static offset (Figures 6 and 8). This implies that the elastic and structural properties of the sedimentary layer remained altered.

This account summarizes the two main aspects that have to be addressed in any comprehensive assessment of governing hydromechanical processes. The first aspect is the temporal evolution, i.e., the coincidence of reservoir stimulation and onset of the transient, the delayed peak deformation with respect to the stimulation and the seismic activity, and the overall transient duration. The second aspect is the spatial relationship between the injection depth, location, and size of the volume affected by the induced fluids and seismicity, and the decorrelation and velocity-change patterns in the overlying rock column. A solution to this problem requires a multidisciplinary approach that is beyond the scope of the present study. Despite the current agnosia regarding processes that drive the here-observed coinjection and postinjection dynamics, we reiterate that passive methods can provide important constraints for models of these governing processes. In the following, we put our results into context through collection of the relevant key observations from a range of injection experiments.

Recall that we resolve a robust decorrelation, but there was no consistent velocity-change signal in the 0.1–0.4 Hz range. In contrast, the high-frequency data showed decoherence and relative velocity variations. Our results are compatible with noise-based observations from a stimulation experiment in St. Gallen, Switzerland (Obermann et al., 2015), where water injection triggered critical processes at 4-km depth that led to a similarly significant loss of waveform coherence. We consider this St. Gallen experiment to be independent confirmation of the large decorrelation values obtained for the Basel experiment. In St. Gallen, the variations in the scattering properties were resolved and located at depth using broadband seismometers. Similarly, no velocity changes were resolved at 0.2–0.4 Hz. Our analysis shows that wave propagation is also altered by deformation perhaps around, but certainly above, the stimulated reservoir.

The observed effect on the shallower material can be compared with independent observations of ground deformation. InSAR observations of deformation in response to deep CO_2 injection in the Algerian desert (the In Salah project; e.g., Rutqvist, 2012) showed patterns that suggested an inflation or uplift in response to the pumping of the gas into the ground. The shapes of these patterns are comparable with our dv/v and σ images associated with the transient peak. However, these patterns are in contrast to the strong positive velocity anomaly that followed the Basel stimulation, which is indicative of subsidence. Subsidence is deduced from matching deformation and dv/v patterns at active volcanoes, where material above a deflating cavity, i.e., subsiding material, shows the same velocity anomaly. In contrast, uplifted material above an inflating cavity is characterized by reduced velocities (Duputel et al., 2009; Ueno et al., 2012; Sens-Schönfelder et al., 2014), consistent with the In Salah observations.

Considering the deep-shallow interaction, we find that the noise-based estimates of the induced velocity change in Basel are generally compatible with images obtained with a 4D earthquake tomography of the geothermal system in Soultz-sous-Forêts, located at the French-German border. Stimulation of two wells caused a decrease in the wave speed in a volume associated with the seismicity distribution around the well head (Calò et al., 2011; Calò and Dorbath, 2013), similar to previous observations of injection responses (Bokelmann and Harjes, 2000). The velocity-change distribution is comparable with the extension of the increased wave speeds in Basel. A consistent feature is that the magnitude of the wave-speed change in both cases is larger than the region of the induced seismicity and that the surrounding material is characterized by opposite velocity changes. The difference in polarity between the two observations is of course significant, and it indicates that different mechanisms act at different depths. Explaining this polarity change is therefore important, to provide an understanding of the interactions between reservoir stimulation and variations in the deformation state in the overlying rock mass.

We consider the St. Gallen, Basel, and Soultz-sous-Forêts analyses as complementary, not contradictory. Observations in St. Gallen and Soultz-sous-Forêts reflect processes in the stimulated volume that coincide with induced seismicity at 4–5 km depth. Again, our decorrelation results in the microseisms frequency band are generally compatible considering the depth regime of the resolved changes. However, an important aspect of the Basel response that distinguishes it from previous observations is the delayed timing of the deformation transient. We conclude with a conceptual model that integrates the key observations and potential governing processes at the Basel site.

It is clear that a diffusive pore-pressure model cannot explain the observed shallow deformation pattern. Coupling injection-rate data to the diffusion model adopted by Goertz-Allmann et al. (2011), we estimate that 20 days after the injection, during the peak dv/v and dc variations, the pressure changes 4 km above the open hole were on the order of 10^{-20} MPa. A purely elastic response that transmits the reservoir pressure state immediately to shallower depths can be ruled out because of the temporal inconsistency. Moreover, an increase in deep pressure is usually associated with inflation, which is not compatible with the subsidence-indicating positive velocity changes. Fluid migration through fractured, opened pathways within the crystalline basement can potentially address some of the time-dependent variability. Leaking gas had a major role in the failure of the St. Gallen experiment (Obermann et al., 2015).

We propose an observation-based scenario that accounts for the delayed, aseismic upward-migrating subsidence triggered by the Basel stimulation. Pressurized fluids can alter the stress state (Goertz-Allmann et al., 2011; Bachmann et al., 2012) and trigger earthquakes at depth (Häring et al., 2008; Deichmann and Giardini, 2009; Kraft and Deichmann, 2014). However, the pressure increase was too small to induce significant inflation. Instead, the damaged volume characterized by reduced wave speeds (Calò et al., 2011; Calò and Dorbath, 2013; Shalev et al., 2013) might yield, which causes the overlying material to sag or subside in an upward-migrating order, where fluid migration and pore pressure redistribution appear to have important roles. Damage is maximal during this settling process, and compaction of the subsiding material leads to a rigidity increase and an associated observed velocity increase (Duputel et al., 2009; Sens-Schönfelder et al., 2014). The robustness of the transient decorrelation and velocity change episode T2 (Figure 5d and 5e) suggests further delayed processes that are potentially associated with the stimulation. This implies that reservoir dynamics are not limited to processes accompanied by microseismicity.

We can qualitatively evaluate the proposed interaction between the enhanced reservoir and the observed layer response. We refer to the stress distribution at the surface of a homogeneous, isotropic, Poisson-solid half-space induced by a buried pressure source (Figure 6 in McTigue, 1987). This model is an extension of Mogi's (1958) solution that considered a finite pressure source. Importantly, the radial stress pattern above the source is characterized by a change from compressive to extensional stress away from the center of the depressurized source. This is therefore consistent with the observed positive to negative velocity change pattern relative to the center of our dv/v images and with the observations made at Piton de la Fournaise (Duputel et al., 2009; Sens-Schönfelder et al., 2014).

Considering future applications of passive methods in engineering contexts, an increase in temporal resolution, i.e., an increase in the signal-to-noise ratio of crosscorrelation coda waveforms, can potentially be obtained using shorter and/or overlapping processing windows (Seats et al., 2012). Solution quality can further be improved by considering correlations constructed from all three components if available (Schaff, 2012; Hillers et al., 2014), which might also reveal anisotropic responses (Hillers et al., 2015b). Fluctuations in relative velocity change measurements are attenuated using weighted inversion schemes (Brenguier et al., 2014). Finally, the application of the crosscorrelation technique for the reconstruction of coherent parts of a diffuse, scattered wavefield is not limited to ambient noise. Correlation of earthquake coda (Campillo and Paul, 2003) can provide temporal high-resolution estimates of medium changes (Roux and Ben-Zion, 2014).

CONCLUSIONS

Applying noise-based passive analysis methods, we have presented and discussed the detection, monitoring, and imaging of an aseismic deformation transient in response to the 2006 Basel reservoir stimulation experiment. The transient initiated with the injection, but it peaked some 15 days after shut-in and bleed-off, and after the induced seismicity had ceased. The transient deformation is characterized by upward migration, with peak deformation values estimated in the sedimentary layer above the stimulated crystalline rock volume, at 4–5 km depth. We verified key observations using multiple analysis and processing techniques. The resolution of an aseismic transient indicates that potentially unwanted reservoir responses are not necessarily accompanied by seismic activity. More detailed modeling efforts are needed to resolve the coupling between fluid injection, damage creation, fluid migration or leakage, seismicity patterns, and delayed transient responses. The very role of fluids in the observed response remains elusive, but our results suggest that the methods used here can help to discern fluid migration by resolving the associated changes in the elastic parameters. Because coda waves have a much higher sensitivity compared with direct waves, these methods constitute a complementary monitoring tool for remote reservoir characterization in a variety of engineering applications, including, but not limited to, mining, fluid injection, and hydraulic fracturing associated with unconventional oil or gas production, nuclear waste management, and CO_2 storage. The temporal and spatial resolution of passive methods can be enhanced by considering intermittent or continuously active sources for excitation of the energetic high-frequency scattered wavefields.

ACKNOWLEDGMENTS

We are grateful to M. O. Häring and O. Genoni of Geothermal Exlorers Ltd., who provided access to continuous waveform data from the borehole stations. Access to continuous waveform data from the surface stations was given by the Swiss Seismological Service at ETH Zurich. G. Hillers is supported by a Heisenberg Fellowship from the German Research Foundation (HI 1714/1-1). This study was supported by the European Research Council (Advanced Grant Whisper L27507). A. Obermann acknowledges funding from the European Community Seventh Framework Programme, under grant agreement no. 608553 (Project IMAGE). The figures were constructed using GMT (Wessel and Smith, 1998). We thank X. Briand for his computational assistance that underpinned much of this work, and T. Kraft and S. Baisch for their helpful comments. We thank the editor and two anonymous reviewers for comments that helped to improve the manuscript.

REFERENCES

Bachmann, C. E., S. Wiemer, B. P. Goertz-Allmann, and J. Woessner, 2012, Influence of pore-pressure on the event-size distribution of induced earthquakes: Geophysical Research Letters, **39**, L09302, doi: 10.1029/2012GL051480.

Bachmann, C. E., S. Wiemer, J. Woessner, and S. Hainzl, 2011, Statistical analysis of the induced Basel 2006 earthquake sequence: Introducing a probability-based monitoring approach for enhanced geothermal systems: Geophysical Journal International, **186**, 793–807, doi: 10.1111/j.1365-246X.2011.05068.x.

Baig, A. M., M. Campillo, and F. Brenguier, 2009, Denoising seismic noise correlations: Journal of Geophysical Research, **114**, B08310, doi: 10.1029/2008JB006085.

Baisch, S., and G. H. R. Bokelmann, 2001, Seismic waveform attributes before and after the Loma Prieta earthquake: Scattering change near the earthquake and temporal recovery: Journal of Geophysical Research, **106**, 16323–16337, doi: 10.1029/2001JB000151.

Bensen, G. D., M. H. Ritzwoller, M. P. Barmin, A. L. Levshin, F. Lin, M. P. Moschetti, N. M. Shapiro, and Y. Yang, 2007, Processing seismic ambient noise data to obtain reliable broad-band surface wave dispersion measurements: Geophysical Journal International, **169**, 1239–1260, doi: 10.1111/j.1365-246X.2007.03374.x.

Bokelmann, G. H. R., and H.-P. Harjes, 2000, Evidence for temporal variation of seismic velocity within the upper continental crust: Journal of Geophysical Research, **105**, 23879–23894, doi: 10.1029/2000JB900207.

Boué, P., P. Poli, M. Campillo, H. Pedersen, X. Briand, and P. Roux, 2013, Teleseismic correlations of ambient seismic noise for deep global imaging of the earth: Geophysical Journal International, **194**, 844–848, doi: 10.1093/gji/ggt160.

Brenguier, F., M. Campillo, C. Hadziioannou, N. M. Shapiro, R. M. Nadeau, and E. Larose, 2008a, Postseismic relaxation along the San Andreas fault at Parkfield from continuous seismological observations: Science, **321**, 1478–1481, doi:10.1126/science.1160943.

Brenguier, F., M. Campillo, T. Takeda, Y. Aoki, N. M. Shapiro, X. Briand, K. Emoto, and H. Miyake, 2014, Mapping pressurized volcanic fluids from induced crustal seismic velocity drops: Science, **345**, 80–82, doi: 10.1126/science.1254073.

Brenguier, F., N. M. Shapiro, M. Campillo, V. Ferrazzini, Z. Duputel, O. Coutant, and A. Nercessian, 2008b, Towards forecasting volcanic eruptions using seismic noise: Nature Geoscience, **1**, 126–130, doi: 10.1038/ngeo104.

Calò, M., and C. Dorbath, 2013, Different behaviours of the seismic velocity field at Soultzsous-Forets revealed by 4-D seismic tomography: Case study of GPK3 and GPK2 injection tests: Geophysical Journal International, **194**, 1119–1137, doi: 10.1093/gji/ggt153.

Calò, M., C. Dorbath, F. H. Cornet, and N. Cuenot, 2011, Large-scale aseismic motion identified through 4-D P-wave tomography: Geophysical Journal International, **186**, 1295–1314, doi: 10.1111/j.1365-246X.2011.05108.x.

Campillo, M., 2006, Phase and correlation of 'random' seismic fields and the reconstruction of the Green function: Pure and Applied Geophysics, **163**, 475–502, doi: 10.1007/s00024-005-0032-8.

Campillo, M., and A. Paul, 2003, Long-range correlations in the diffuse seismic coda: Science, **299**, 547–549, doi: 10.1126/science.1078551.

Campillo, M., H. Sato, N. M. Shapiro, and R. D. van der Hilst, 2011, New developments on imaging and monitoring with seismic noise:

Comptes Rendus Geoscience, **343**, 487–495, doi: 10.1016/j.crte.2011.07.007.
Catalli, F., M.-A. Meier, and S. Wiemer, 2013, The role of Coulomb stress changes for injection-induced seismicity: The Basel enhanced geothermal system: Geophysical Research Letters, **40**, 72–77, doi: 10.1029/2012GL054147.
Clarke, D., L. Zaccarelli, N. M. Shapiro, and F. Brenguier, 2011, Assessment of resolution and accuracy of the moving window cross spectral technique for monitoring crustal temporal variations using ambient seismic noise: Geophysical Journal International, **186**, 867–882, doi: 10.1111/j.1365-246X.2011.05074.x.
Colombi, A., J. Chaput, F. Brenguier, G. Hillers, P. Roux, and M. Campillo, 2014, On the temporal stability of the coda of ambient noise correlations: Comptes Rendus Geoscience, **346**, 307–316, doi: 10.1016/j.crte.2014.10.002.
Deichmann, N., and J. Ernst, 2009, Earthquake focal mechanisms of the induced seismicity in 2006 and 2007 below Basel (Switzerland): Swiss Journal of Geoscience, **102**, 457–466, doi: 10.1007/s00015-009-1336-y.
Deichmann, N., and D. Giardini, 2009, Earthquakes induced by the stimulation of an enhanced geothermal system below Basel (Switzerland): Seismological Research Letters, **80**, 784–798, doi: 10.1785/gssrl.80.5.784.
Duputel, Z., V. Ferrazzini, F. Brenguier, N. Shapiro, M. Campillo, and A. Nercessian, 2009, Real time monitoring of relative velocity changes using ambient seismic noise at the Piton de la Fournaise volcano (La Réunion) from January 2006 to June 2007: Journal of Volcanology and Geothermal Research, **184**, 164–173, doi: 10.1016/j.jvolgeores.2008.11.024.
Dyer, B. C., U. Schanz, T. Spillmann, F. Ladner, and M. O. Häring, 2010, Application of microseismic multiplet analysis to the Basel geothermal reservoir stimulation events: Geophysical Prospecting, **58**, 791–807, doi: 10.1111/j.1365-2478.2010.00902.x.
Ellsworth, W. L., 2013, Injection-induced earthquakes: Science, **341**, 6142, doi: 10.1126/science.1225942.
Froment, B., M. Campillo, J. H. Chen, and Q. Y. Liu, 2013, Deformation at depth associated with the 12 May 2008 Mw 7.9 Wenchuan earthquake from seismic ambient noise monitoring: Geophysical Research Letters, **40**, 78–82, doi: 10.1029/2012GL053995.
Froment, B., M. Campillo, P. Roux, P. Gouédard, A. Verdel, and R. L. Weaver, 2010, Estimation of the effect of nonisotropically distributed energy on the apparent arrival time in correlations: Geophysics, **75**, no. 5, SA85–SA93, doi: 10.1190/1.3483102.
Giardini, D., 2009, Geothermal quake risks must be faced: Nature, **462**, 848–849, doi: 10.1038/462848a.
Goertz-Allmann, B. P., A. Goertz, and S. Wiemer, 2011, Stress drop variations of induced earthquakes at the Basel geothermal site: Geophysical Research Letters, **38**, L09308, doi: 10.1029/2011GL047498.
Goertz-Allmann, B. P., and S. Wiemer, 2013, Geomechanical modeling of induced seismicity source parameters and implications for seismic hazard assessment: Geophysics, **78**, no. 1, KS25–KS39, doi: 10.1190/geo2012-0102.1.
Hadziioannou, C., E. Larose, O. Coutant, P. Roux, and M. Campillo, 2009, Stability of monitoring weak changes in multiply scattering media with ambient noise correlations: Laboratory experiments: Journal of the Acoustical Society of America, **125**, 3688–3695, doi: 10.1121/1.3125345.
Hansen, P. C., 1992, Analysis of discrete ill-posed problems by means of the L-curve: SIAM Review, **34**, 561–580, doi: 10.1137/1034115.
Häring, M. O., U. Schanz, F. Ladner, and B. C. Dyer, 2008, Characterisation of the Basel 1 enhanced geothermal system: Geothermics, **37**, 469–495, doi: 10.1016/j.geothermics.2008.06.002.
Hennino, R., N. Trégourès, N. M. Shapiro, L. Margerin, M. Campillo, B. A. van Tiggelen, and R. L. Weaver, 2001, Observation of equipartitioning of seismic waves: Physical Review Letters, **86**, 3447–3450, doi: 10.1103/PhysRevLett.86.3447.
Herrmann, R. B., 2006, Computer programs in seismology, vers. 3.30: An overview of synthetic seismogram computation, Technical report, Saint Louis University.
Hillers, G., Y. Ben-Zion, M. Campillo, and D. Zigone, 2015a, Seasonal variations of seismic velocities in the San Jacinto fault area observed with ambient seismic noise: Geophysical Journal International, doi: 10.1093/gji/ggv151.
Hillers, G., Y. Ben-Zion, M. Landès, and M. Campillo, 2013, Interaction of microseisms with crustal heterogeneity: A case study from the San Jacinto fault zone area: Geochemistry, Geophysics, Geosystems, **14**, 2182–2197, doi: 10.1002/ggge.20140.
Hillers, G., M. Campillo, Y.-Y. Lin, K.-F. Ma, and P. Roux, 2012a, Anatomy of the high-frequency ambient seismic wave field at the TCDP borehole: Journal of Geophysical Research, **117**, B06301, doi: 10.1029/2011JB008999.
Hillers, G., M. Campillo, and K.-F. Ma, 2014, Seismic velocity variations at TCDP are controlled by MJO driven precipitation pattern and high fluid discharge properties: Earth and Planetary Science Letters, **391**, 121–127, doi: 10.1016/j.epsl.2014.01.040.
Hillers, G., N. Graham, M. Campillo, S. Kedar, M. Landes, and N. Shapiro, 2012b, Global oceanic microseism sources as seen by seismic arrays and predicted by wave action models: Geochemistry, Geophysics, Geosystems, **13**, Q01021, doi: 10.1029/2011GC003875.
Hillers, G., L. Retailleau, M. Campillo, A. Inbal, J.-P. Ampuero, and T. Nishimura, 2015b, In situ observations of velocity changes in response to tidal deformation from analysis of the high-frequency ambient wavefield: Journal of Geophysical Research, **120**, 210–225, doi: 10.1002/2014JB011318.
Hobiger, M., U. Wegler, K. Shiomi, and H. Nakahara, 2012, Coseismic and postseismic elastic wave variations caused by the 2008 Iwate-Miyagi Nairiku earthquake, Japan: Journal of Geophysical Research, **117**, B09313, doi: 10.1029/2012JB009402.
Husen, S., E. Kissling, and J. F. Clinton, 2011, Local and regional minimum 1D models for earthquake location and data quality assessment in complex tectonic regions: Application to Switzerland: Swiss Journal of Geoscience, **104**, 455–469.
Julian, B. R., and G. R. Foulger, 2010, Time-dependent seismic tomography: Geophysical Journal International, **182**, 1327–1338, doi: 10.1111/j.1365-246X.2010.04668.x.
Kastrup, U., M. L. Zoback, N. Deichmann, K. F. Evans, D. Giardini, and A. J. Michael, 2004, Stress field variations in the Swiss Alps and the northern Alpine foreland derived from inversion of fault plane solutions: Journal of Geophysical Research, **109**, B01402, doi: 10.1029/2003JB002550.
Koch, K., and K. Stammler, 2003, Detection and elimination of time synchronization problems for the GERESS array by correlating microseismic noise: Seismological Research Letters, **74**, 803–816, doi: 10.1785/gssrl.74.6.803.
Kraft, T., and N. Deichmann, 2014, High-precision relocation and focal mechanism of the injection-induced seismicity at the Basel EGS: Geothermics, **52**, 59–73, doi: 10.1016/j.geothermics.2014.05.014.
Lacombe, C., M. Campillo, A. Paul, and L. Margerin, 2003, Separation of intrinsic absorption and scattering attenuation from *Lg* coda decay in central France using acoustic radiative transfer theory: Geophysical Journal International, **154**, 417–425, doi: 10.1046/j.1365-246X.2003.01976.x.
Larose, E., T. Planès, V. Rossetto, and L. Margerin, 2010, Locating a small change in a multiple scattering environment: Applied Physics Letters, **96**, 204101, doi: 10.1063/1.3431269.
Larose, E., P. Roux, and M. Campillo, 2007, Reconstruction of Rayleigh-Lamb dispersion spectrum based on noise obtained from an air-jet forcing: Journal of the Acoustical Society of America, **122**, 3437–3444, doi: 10.1121/1.2799913.
Lobkis, O. I., and R. L. Weaver, 2001, On the emergence of the Green's function in the correlations of a diffuse field: Journal of the Acoustical Society of America, **110**, 3011–3017, doi: 10.1121/1.1417528.
Lobkis, O. I., and R. L. Weaver, 2003, Coda-wave interferometry in finite solids: Recovery of P-to-S conversion rates in an elastodynamic billiard: Physical Review Letters, **90**, 25–27, doi: 10.1103/PhysRevLett.90.254302.
Margerin, L., M. Campillo, B. A. van Tiggelen, and R. Hennino, 2009, Energy partition of seismic coda waves in layered media: Theory and application to Pinyon flats observatory: Geophysical Journal International, **177**, 571–585, doi: 10.1111/j.1365-246X.2008.04068.x.
McTigue, D. F., 1987, Elastic stress and deformation near a finite spherical magma body: Resolution of the point source paradox: Journal of Geophysical Research, **92**, 12931–12940, doi: 10.1029/JB092iB12p12931.
Meier, U., N. M. Shapiro, and F. Brenguier, 2010, Detecting seasonal variations in seismic velocities within Los Angeles basin from correlations of ambient seismic noise: Geophysical Journal International, **181**, 985–996, doi: 10.1111/j.1365-246X.2010.04550.x.
Michaels, J. E., and T. E. Michaels, 2005, Detection of structural damage from the local temporal coherence of diffuse ultrasonic signals: IEEE Transactions on Ultrasonics, Ferroelectrics and Frequency Control, **52**, 1769–1782, doi: 10.1109/TUFFC.2005.1561631.
Mogi, K., 1958, Relations between the eruptions of various volcanoes and the deformations of the ground surface around them: Bulletin of the Earthquake Research Institute, University of Tokyo, **36**, 99–134.
Mordret, A., N. M. Shapiro, S. S. Singh, P. Roux, and O. I. Barkved, 2013, Helmholtz tomography of ambient noise surface wave data to estimate Scholte wave phase velocity at Valhall Life of the Field: Geophysics, **78**, no. 2, WA99–WA109, doi: 10.1190/geo2012-0303.1.
Obermann, A., B. Froment, M. Campillo, E. Larose, T. Planès, B. Valette, J. H. Chen, and Q. Y. Liu, 2014, Seismic noise correlations to image structural and mechanical changes associated with the Mw 7.9 2008 Wenchuan earthquake: Journal of Geophysical Research, **119**, 3155–3168, doi: 10.1002/2013JB010932.
Obermann, A., T. Kraft, E. Larose, and S. Wiemer, 2015, Potential of ambient seismic noise techniques to monitor the St. Gallen geothermal site (Switzerland): Journal of Geophysical Research, doi: 10.1002/2014JB011817.
Obermann, A., T. Planès, E. Larose, and M. Campillo, 2013a, Imaging preeruptive and coeruptive structural and mechanical changes of a volcano

with ambient seismic noise: Journal of Geophysical Research, **118**, 6285–6294, doi: 10.1002/2013JB010399.
Obermann, A., T. Planès, E. Larose, C. Sens-Schönfelder, and M. Campillo, 2013b, Depth sensitivity of seismic coda waves to velocity perturbations in an elastic heterogeneous medium: Geophysical Journal International, **194**, 372–382, doi: 10.1093/gji/ggt043.
Paasschens, J. C. J., 1997, Solution of the time-dependent Boltzmann equation: Physical Review E, **56**, 1135–1141, doi: 10.1103/PhysRevE.56.1135.
Pacheco, C., and R. Snieder, 2005, Time-lapse travel time change of multiply scattered acoustic waves: Journal of the Acoustical Society of America, **118**, 1300–1310, doi: 10.1121/1.2000827.
Paul, A., M. Campillo, L. Margerin, E. Larose, and A. Derode, 2005, Empirical synthesis of time-asymmetrical Green function from the correlation of coda waves: Journal of Geophysical Research, **110**, B08302, doi: 10.1029/2004JB003521.
Planès, T., E. Larose, L. Margerin, V. Rossetto, and C. Sens-Schonfelder, 2014, Decorrelation and phase-shift of coda waves induced by local changes: Multiple scattering approach and numerical validation: Waves in Random and Complex Media, **24**, 99–125, doi: 10.1080/17455030.2014.880821.
Planès, T., E. Larose, V. Rossetto, and L. Margerin, 2015, Imaging multiple local changes in heterogeneous media with diffuse waves: Journal of the Acoustical Society of America, **137**, 660–667, doi: 10.1121/1.4906824.
Poli, P., H. A. Pedersen, and M. Campillo, and the POLENET/LAPNET Working Group, 2012, Emergence of body waves from cross-correlation of short period seismic noise: Geophysical Journal International, **188**, 549–558, doi: 10.1111/j.1365-246X.2011.05271.x.
Poupinet, G., W. Ellsworth, and J. Frechet, 1984, Monitoring velocity variations in the crust using earthquake doublets: An application to the Calaveras Fault, California: Journal of Geophysical Research, **89**, 5719–5731, doi: 10.1029/JB089iB07p05719.
Richter, T., C. Sens-Schönfelder, R. Kind, and G. Asch, 2014, Comprehensive observation and modeling of earthquake and temperature-related seismic velocity changes in northern Chile with passive image interferometry: Journal of Geophysical Research, **119**, 4747–4765, doi: 10.1002/2013JB010695.
Rivet, D., M. Campillo, N. M. Shapiro, V. Cruz-Atienza, M. Radiguet, N. Cotte, and V. Kostoglodov, 2011, Seismic evidence of nonlinear crustal deformation during a large slow slip event in Mexico: Geophysical Research Letters, **38**, L08308, doi: 10.1029/2011GL047151.
Rossetto, V., L. Margerin, T. Planès, and E. Larose, 2011, Locating a weak change using diffuse waves: Theoretical approach and inversion procedure: Journal of Applied Physics, **109**, 034903, doi: 10.1063/1.3544503.
Roux, P., and Y. Ben-Zion, 2014, Monitoring fault zone environments with correlations of earthquake waveforms: Geophysical Journal International, **196**, 1073–1081, doi: 10.1093/gji/ggt441.
Roux, P., K. G. Sabra, W. A. Kuperman, and A. Roux, 2005, Ambient noise cross correlation in free space: Theoretical approach: Journal of the Acoustical Society of America, **117**, 79–84, doi: 10.1121/1.1830673.
Rutqvist, J., 2012, The geomechanics of CO_2 storage in deep sedimentary formations: Geotechnical and Geological Engineering, **30**, 525–551, doi: 10.1007/s10706-011-9491-0.
Sánchez-Sesma, F. J., and M. Campillo, 2006, Retrieval of the Green's function from cross correlation: The canonical elastic problem: Bulletin of the Seismological Society of America, **96**, 1182–1191, doi: 10.1785/0120050181.
Sato, H., 1993, Energy transportation in one- and two-dimensional scattering media: Analytic solutions of the multiple isotropic scattering model: Geophysical Journal International, **112**, 141–146, doi: 10.1111/j.1365-246X.1993.tb01443.x.
Sato, H., M. C. Fehler, and T. Maeda (Eds.), 2012, Seismic wave propagation and scattering in the heterogeneous earth, 2nd ed.: Springer.
Schaff, D. P., 2012, Placing an upper bound on preseismic velocity changes measured by ambient noise monitoring for the 2004 M_w 6.0 Parkfield earthquake (California): Bulletin of the Seismological Society of America, **102**, 1400–1416, doi: 10.1785/0120110342.
Schoenball, M., L. Dorbath, E. Gaucher, J. F. Wellmann, and T. Kohl, 2014, Change of stress regime during geothermal reservoir stimulation: Geophysical Research Letters, **41**, 1163–1170, doi: 10.1002/2013GL058514.
Seats, K. J., J. F. Lawrence, and G. A. Prieto, 2012, Improved ambient noise correlation functions using Welch's method: Geophysical Journal International, **188**, 513–523, doi: 10.1111/j.1365-246X.2011.05263.x.
Sens-Schönfelder, C., and E. Larose, 2008, Temporal changes in the lunar soil from correlation of diffuse vibrations: Physical Review E, **78**, 045601, doi: 10.1103/PhysRevE.78.045601.
Sens-Schönfelder, C., E. Pomponi, and A. Peltier, 2014, Dynamics of Piton de la Fournaise volcano observed by passive image interferometry with multiple references: Journal of Volcanology and Geothermal Research, **276**, 32–45, doi: 10.1016/j.jvolgeores.2014.02.012.
Sens-Schönfelder, C., and U. Wegler, 2006a, Passive image interferometry and seasonal variations of seismic velocities at Merapi volcano, Indonesia: Geophysical Research Letters, **33**, L21302, doi: 10.1029/2006GL027797.
Sens-Schönfelder, C., and U. Wegler, 2006b, Radiative transfer theory for estimation of the seismic moment: Geophysical Journal International, **167**, 1363–1372, doi: 10.1111/j.1365-246X.2006.03139.x.
Shalev, E., M. Calò, and V. Lyakhovsky, 2013, Formation of damage zone and seismic velocity variations during hydraulic stimulation: Numerical modelling and field observations: Geophysical Journal International, **195**, 1023–1033, doi: 10.1093/gji/ggt279.
Shang, T., and L. Gao, 1988, Transportation theory of multiple scattering and its application to seismic coda waves of impulsive source: Science Sinica, **31**, 1503–1514.
Shapiro, S. A., 2008, Microseismicity: A tool for reservoir characterization: EAGE Publications bv.
Shapiro, S. A., C. Dinske, and J. Kummerow, 2007, Probability of a given-magnitude earthquake induced by a fluid injection: Geophysical Research Letters, **34**, L22314, doi: 10.1029/2007GL031615.
Shapiro, S. A., O. S. Krüger, C. Dinske, and C. Langenbruch, 2011, Magnitudes of induced earthquakes and geometric scales of fluid-stimulated rock volumes: Geophysics, **76**, no. 6, WC55–WC63, doi:10.1190/geo2010-0349.1.
Snieder, R., 2007, Extracting the Greens function of attenuating heterogeneous acoustic media from uncorrelated waves: Journal of the Acoustical Society of America, **121**, 2637–2643, doi: 10.1121/1.2713673.
Snieder, R., and E. Larose, 2013, Extracting earth's elastic wave response from noise measurements: Annual Review of Earth Planet Science, **41**, 183–206, doi: 10.1146/annurev-earth-050212-123936.
Stehly, L., M. Campillo, and N. M. Shapiro, 2006, A study for the seismic noise from its long-range correlation properties: Journal of Geophysical Research, **111**, B10306, doi: 10.1029/2005JB004237.
Stehly, L., P. Cupillard, and B. Romanowicz, 2011, Towards improving ambient noise tomography using simultaneously curvelet denoising filters and SEM simulations of seismic ambient noise: Comptes Rendus Geoscience, **343**, 591–599, doi: 10.1016/j.crte.2011.03.005.
Tarantola, A., and B. Valette, 1982, Generalized nonlinear inverse problems solved using the least squares criterion: Reviews of Geophysics, **20**, 219–232, doi: 10.1029/RG020i002p00219.
Terakawa, T., S. A. Miller, and N. Deichmann, 2012, High fluid pressure and triggered earthquakes in the enhanced geothermal system in Basel, Switzerland: Journal of Geophysical Research, **117**, B07305, doi: 10.1029/2011JB008980.
Ueno, T., T. Saito, K. Shiomi, B. Enescu, H. Hirose, and K. Obara, 2012, Fractional seismic velocity change related to magma intrusions during earthquake swarms in the eastern Izu peninsula, central Japan: Journal of Geophysical Research, **117**, B12305, doi: 10.1029/2012JB009580.
Wapenaar, K., 2004, Retrieving the elastodynamic Greens function of an arbitrary inhomogeneous medium by cross correlation: Physical Review Letters, **93**, 254–301, doi: 10.1103/PhysRevLett.93.254301.
Weaver, R. L., B. Froment, and M. Campillo, 2009, On the correlation of non-isotropically distributed ballistic scalar diffuse waves: Journal of the Acoustical Society of America, **126**, 1817–1826, doi: 10.1121/1.3203359.
Weaver, R. L., C. Hadziioannou, E. Larose, and M. Campillo, 2011, On the precision of noise correlation interferometry: Geophysical Journal International, **185**, 1384–1392, doi: 10.1111/j.1365-246X.2011.05015.x.
Wegler, U., H. Nakahara, C. Sens-Schönfelder, M. Korn, and K. Shiomi, 2009, Sudden drop of seismic velocity after the 2004 Mw 6.6 mid-Niigata earthquake, Japan, observed with passive image interferometry: Journal of Geophysical Research, **114**, B06305, doi: 10.1029/2008JB005869.
Wegler, U., and C. Sens-Schönfelder, 2007, Fault zone monitoring with passive image interferometry: Geophysical Journal International, **168**, 1029–1033, doi: 10.1111/j.1365-246X.2006.03284.x.
Wessel, P., and W. H. F. Smith, 1998, New, improved version of generic mapping tools released: Eos — Transactions of the American Geophysical Union, **79**, 579, 10.1029/98EO00426.
Zhan, Z., V. C. Tsai, and R. W. Clayton, 2013, Spurious velocity changes caused by temporal variations in ambient noise frequency content: Geophysical Journal International, **194**, 1574–1581, doi: 10.1093/gji/ggt170.